STOCHSYNC: STOCHASTIC DIFFUSION SYNCHRONIZATION FOR IMAGE GENERATION IN ARBITRARY SPACES

Kyeongmin Yeo* **Jaihoon Kim*** **Minhyuk Sung**
KAIST
{aaaaa, jh27kim, mhsung}@kaist.ac.kr

Figure 1: Assorted mesh textures and panoramas generated using `StochSync`. `StochSync` extends the capabilities of image diffusion models trained in square spaces to produce images in arbitrary spaces such as cylinders, spheres, tori, and mesh surfaces.

ABSTRACT

We propose a zero-shot method for generating images in arbitrary spaces (e.g., a sphere for 360° panoramas and a mesh surface for texture) using a pretrained image diffusion model. The zero-shot generation of various visual content using a pretrained image diffusion model has been explored mainly in two directions. First, Diffusion Synchronization–performing reverse diffusion processes jointly across different projected spaces while synchronizing them in the target space–generates high-quality outputs when enough conditioning is provided, but it struggles in its absence. Second, Score Distillation Sampling–gradually updating the target space data through gradient descent–results in better coherence but often lacks detail. In this paper, we reveal for the first time the interconnection between these two methods while highlighting their differences. To this end, we propose `StochSync`, a novel approach that combines the strengths of both, enabling effective performance with weak conditioning. Our experiments demonstrate that `StochSync` provides the best performance in 360° panorama generation (where image conditioning is not given), outperforming previous finetuning-based methods, and also delivers comparable results in 3D mesh texturing (where depth conditioning is provided) with previous methods.

1 INTRODUCTION

Diffusion models pretrained on billions of images have shown impressive zero-shot capabilities, generating arbitrary-sized images (Bar-Tal et al., 2023; Lee et al., 2023), 3D mesh textures (Cao et al., 2023), ambiguous images (Geng et al., 2024b), and zoomed-in images (Wang et al., 2024a; Geng et al., 2024a). This cross-domain generation is achieved by mapping from the model's native *instance space* (e.g., a 2D square image) to a target *canonical space* (e.g., a cylinder for 360° panoramas or a 3D mesh for texture generation), as illustrated in Fig. 1. This approach avoids the need for new data collection or separate generative models for each type of data.

*Equal contribution

Two main strategies have been proposed to address this problem. Diffusion Synchronization (DS) (Bar-Tal et al., 2023; Kim et al., 2024a) jointly performs the reverse process of diffusion models across multiple instance spaces while synchronizing their intermediate outputs in the canonical space, but it often suffers from convergence issues and visible seams when strong conditioning is absent. In contrast, Score Distillation Sampling (SDS) (Poole et al., 2023) and its variants (Lukoianov et al., 2024; Liang et al., 2024) update the canonical space via gradient descent from instance spaces, offering robustness in unconditional settings at the cost of realism.

In this work, we introduce Stochastic Diffusion Synchronization (`StochSync`), which fuses the strengths of DS and SDS. We show that each SDS step can be interpreted as a one-step DDIM refinement that maximizes stochasticity in the denoising process. By incorporating this stochasticity into DS, we achieve better coherence across views and eliminate seam artifacts. To further enhance realism, we propose improved clean sample prediction via multi-step denoising and the use of non-overlapping view sampling strategy. Experiments on 360° panoramic image and mesh texture generation confirm that `StochSync` outperforms previous zero-shot and finetuning-based methods, mitigating issues such as overfitting and geometric distortions.

2 Related Work

Panorama Generation. With the release of image diffusion models trained on large-scale datasets (Rombach et al., 2022), methods that leverage these pretrained models for text-conditioned panorama generation have gained attention. MVDiffusion (Tang et al., 2023) and PanFusion (Zhang et al., 2024a) finetune these pretrained models using a panoramic images dataset (Chang et al., 2017). However, finetuning diffusion models on a small dataset risks overfitting, reducing their generalizability. In contrast, SyncTweedies (Kim et al., 2024a) employs DS for zero-shot panorama generation but relies on depth map conditions, which are not commonly available in practice. L-MAGIC (Cai et al., 2024), on the other hand, adopts an inpainting diffusion model, sequentially filling in the panoramic images. However, this iterative process cannot refine previous predictions, leading to error accumulation and often resulting in wavy panoramas.

Mesh Texturing. 3D mesh texturing using image diffusion models has gained significant attention. Among these approaches, Paint3D (Zeng et al., 2024) finetunes a pretrained diffusion model on a synthetic 3D mesh dataset (Deitke et al., 2023), but this often results in unrealistic texture images due to overfitting to the synthetic dataset. For zero-shot approaches, previous works have utilized SDS to update the texture of 3D meshes (Metzer et al., 2023; Chen et al., 2023b; Youwang et al., 2023). DS is also widely used for 3D mesh texturing, with previous works (Liu et al., 2023; Zhang et al., 2024b; Kim et al., 2024a) averaging the one-step predicted clean samples across multiple denoising processes. Another line of research explores the outpainting approach (Chen et al., 2023a; Richardson et al., 2023), where the 3D mesh is textured iteratively, often resulting in textures with visible seams.

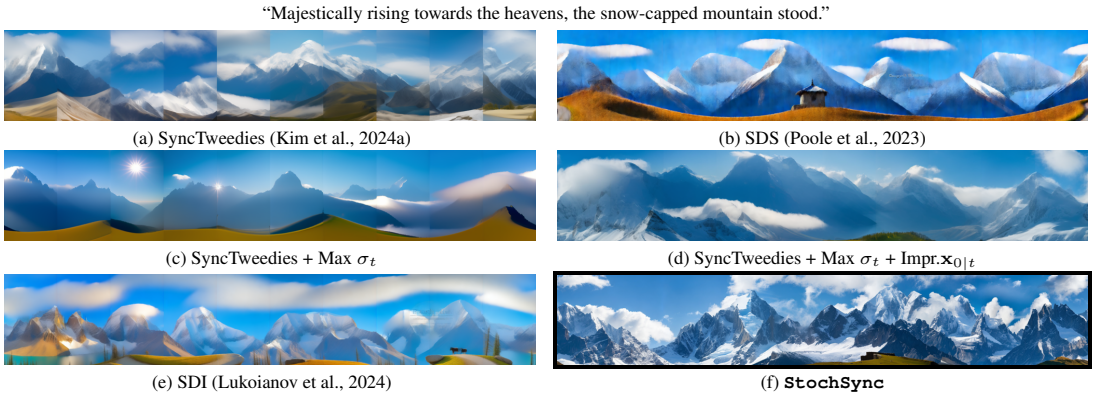

(a) SyncTweedies (Kim et al., 2024a)
(b) SDS (Poole et al., 2023)
(c) SyncTweedies + Max σ_t
(d) SyncTweedies + Max σ_t + Impr.$\mathbf{x}_{0|t}$
(e) SDI (Lukoianov et al., 2024)
(f) **StochSync**

Figure 2: A comparison of SyncTweedies (Kim et al., 2024a), a synchronization method, SDS (Poole et al., 2023), and `StochSync` which uses SyncTweedies as a base and incorporates maximum stochasticity (Max σ_t), multi-step $\mathbf{x}_{0|t}$ computation (Impr. $\mathbf{x}_{0|t}$), and non-overlapping view sampling (N.O. Views), alongside others that use only a subset of these components.

3 Problem Definition and Overview

We propose a method for generating data points in one space (referred to as the *canonical space* $\mathcal{Z}$) using a pretrained diffusion model that has been trained on *another space* (referred to as the instance space $\mathcal{X}$),

where the mapping from the canonical space to the instance space is known. For example, the canonical space could be a sphere representing 360° panoramas, or a 3D mesh surface for creating mesh textures, and the instance space is a 2D square, the space for most pretrained image diffusion models. In general, a region of the canonical space is mapped to the instance space through a specific view. The mapping from a region of the canonical space to the instance space through a view $\mathbf{c}$ is represented by the projection operation $f_{\mathbf{c}}(\mathbf{z}) : \mathcal{Z}_{\mathbf{c}} \to \mathcal{X}$, where $\mathbf{z} \in \mathcal{Z}_{\mathbf{c}} \subseteq \mathcal{Z}$. Our objective is to produce realistic data points in the canonical space without using any generative model trained on samples in that space, but by leveraging pretrained diffusion models in the instance spaces and their multiple denoising processes from different views. This approach can extend the capabilities of pretrained diffusion models to produce diverse types of data, eliminating the need to collect large-scale data and train separate generative models.

4 Diffusion Reverse Process

The forward process of a diffusion model (Sohl-Dickstein et al. (2015); Ho et al. (2020); Song et al. (2021b)) sequentially corrupts sample data using a predefined variance schedule $\alpha_1, \ldots, \alpha_T$, where one can sample $\mathbf{x}_t$ at arbitrary timestep t from a clean sample $\mathbf{x}_0$:

$$\mathbf{x}_t = \sqrt{\alpha_t}\mathbf{x}_0 + \sqrt{1-\alpha_t}\boldsymbol{\epsilon}, \quad \text{where} \quad \boldsymbol{\epsilon} \sim \mathcal{N}(\mathbf{0}, \boldsymbol{I}). \tag{1}$$

Song et al. (2021a) propose DDIM, a diffusion reverse process generalizing DDPM Ho et al. (2020), by defining the posterior distribution $q_{\sigma_t}(\mathbf{x}_{t-1}|\mathbf{x}_t, \mathbf{x}_0)$ with a parameter σ_t determining the level of stochasticity as follows:

$$q_{\sigma_t}(\mathbf{x}_{t-1}|\mathbf{x}_t, \mathbf{x}_0) = \mathcal{N}\left(\mu_{\sigma_t}(\mathbf{x}_0, \mathbf{x}_t), \sigma_t^2 \boldsymbol{I}\right), \tag{2}$$

$$\text{where} \quad \mu_{\sigma_t}(\mathbf{x}_0, \mathbf{x}_t) = \sqrt{\alpha_{t-1}}\mathbf{x}_0 + \sqrt{1-\alpha_{t-1}-\sigma_t^2} \cdot \frac{\mathbf{x}_t - \sqrt{\alpha_t}\mathbf{x}_0}{\sqrt{1-\alpha_t}}. \tag{3}$$

In the reverse process, the noise $\boldsymbol{\epsilon}_t$ is first estimated from $\mathbf{x}_t$ using the noise predictor $\epsilon_\theta(\mathbf{x}_t, y)$, where y is the input condition (e.g., a text prompt). Tweedie's formula (Robbins, 1956) is then applied to approximate the clean sample in Eq. 2, denoted by $\mathbf{x}_{0|t}$:

$$\mathbf{x}_{0|t} = \psi(\mathbf{x}_t, \boldsymbol{\epsilon}_t) = \frac{\mathbf{x}_t - \sqrt{1-\alpha_t}\boldsymbol{\epsilon}_t}{\sqrt{\alpha_t}}. \tag{4}$$

A clean data sample $\mathbf{x}_0$ is then generated by first sampling standard Gaussian noise $\mathbf{x}_T \sim \mathcal{N}(\mathbf{0}, \boldsymbol{I})$ and gradually denoising it over time by iteratively sampling a noisy data point $\mathbf{x}_t$ from $p_\theta(\mathbf{x}_{t-1}|\mathbf{x}_t)$. The mapping from a noisy data point $\mathbf{x}_t$ to $\mathbf{x}_0$ becomes deterministic when $\sigma_t = 0$ for all t and is equivalent to solving an ODE (Song et al., 2021b; Chen et al., 2018) with a specific discretization.

Reverse Process from the Perspective of $\mathbf{x}_{0|t}$. Here, to connect the reverse process of DDIM to the algorithms to be introduced in the next section, we reinterpret the reverse denoising process as an iterative *refinement* process of the prediction of clean sample $\mathbf{x}_{0|t}$. See Alg. 1, where $\mathbf{x}_{0|t}$ and $\boldsymbol{\epsilon}_t$ are computed at each timestep. Note that the mean of the likelihood distribution $p_\theta(\mathbf{x}_{t-1}|\mathbf{x}_t)$ in Eq. 3 can be rewritten in terms of $\mathbf{x}_0$ and $\boldsymbol{\epsilon}_t$:

$$\mu_{\sigma_t}(\mathbf{x}_0, \boldsymbol{\epsilon}_t) = \sqrt{\alpha_{t-1}}\mathbf{x}_0 + \sqrt{1-\alpha_{t-1}-\sigma_t^2} \cdot \boldsymbol{\epsilon}_t. \tag{5}$$

Apart from setting $\sigma_t = 0$, one can consider a special case when $\sigma_t = \sqrt{1-\alpha_{t-1}}$, which maximizes the level of stochasticity during the sampling process. This cancels out the noise prediction term $\boldsymbol{\epsilon}_t$ in Eq. 5. We denote this case by overriding $\mu_{\sigma_t}(\cdot,\cdot)$ with $\mu^*(\cdot)$, which now takes a single parameter $\mathbf{x}_0$:

$$\mu^*(\mathbf{x}_0) = \sqrt{\alpha_{t-1}}\mathbf{x}_0. \tag{6}$$

5 Diffusion Synchronization and Score Distillation Sampling

5.1 Diffusion Synchronization

The idea of Diffusion Synchronization (DS) (Liu et al., 2022; Geng et al., 2024b; Kim et al., 2024a) is to perform the reverse process jointly across multiple instance spaces while synchronizing the processes through mapping to the canonical space. Among the various options for synchronization, Kim et al. (2024a) have demonstrated that averaging the predictions of the clean samples $\mathbf{x}_{0|t}$ in the canonical space

Algorithm 1: Diffusion Reverse Process

Inputs: y: Input text prompt
Outputs: $\mathbf{x}_0$: An instance space sample aligned with y

Function `Reverse Process(y)`:
- $\mathbf{x}_T \sim \mathcal{N}(\mathbf{0}, \boldsymbol{I})$
- $\boldsymbol{\epsilon}_T \leftarrow \epsilon_\theta(\mathbf{x}_T, y)$
- $\mathbf{x}_{0|T} \leftarrow \psi(\mathbf{x}_T, \boldsymbol{\epsilon}_T)$
- **for** $t = T \ldots 2$ **do**
  - $\mathbf{x}_{t-1} \sim \mathcal{N}(\mu_{\sigma_t}(\mathbf{x}_{0|t}, \boldsymbol{\epsilon}_t), \sigma_t^2 \boldsymbol{I})$ // Eq. 5
  - $\boldsymbol{\epsilon}_{t-1} \leftarrow \epsilon_\theta(\mathbf{x}_{t-1}, y)$
  - $\mathbf{x}_{0|t-1} \leftarrow \psi(\mathbf{x}_{t-1}, \boldsymbol{\epsilon}_{t-1})$ // Eq. 4
- **end**

Algorithm 2: Diffusion Synchronization (DS)

Inputs: $\mathbf{z}$: A canonical space sample
y: Input text prompt; $\mathbf{c}^{1:N}$: A set of views.
Outputs: $\mathbf{z}$: Canonical space sample aligned with y

1 **Function** `DS(z, y, c^{1:N})`:
2 $\mathbf{x}_T^{1:N} \sim \mathcal{N}(\mathbf{0}, \boldsymbol{I})$
3 **for** $i = 1 \ldots N$ **do**
4 $\boldsymbol{\epsilon}_T^{(i)} \leftarrow \epsilon_\theta(\mathbf{x}_T^{(i)}, y)$
5 $\mathbf{x}_{0|T}^{(i)} \leftarrow \psi(\mathbf{x}_T^{(i)}, \boldsymbol{\epsilon}_T^{(i)})$ // Eq. 4
6 **end**
7 $\mathbf{z} \leftarrow \arg\min_{\mathbf{z}} \sum_{i=1}^{N} \| f_{\mathbf{c}^{(i)}}(\mathbf{z}) - \mathbf{x}_{0|T}^{(i)} \|^2$
8 **for** $t = T \ldots 2$ **do**
// $\mathbf{c}^{1:N}$ is fixed for all t.
9 **for** $i = 1 \ldots N$ **do**
10 $\mathbf{x}_{0|t}^{(i)} \leftarrow f_{\mathbf{c}^{(i)}}(\mathbf{z})$
11 $\mathbf{x}_{t-1}^{(i)} \sim \mathcal{N}(\mu_{\sigma_t}(\mathbf{x}_{0|t}^{(i)}, \boldsymbol{\epsilon}_t^{(i)}), \sigma_t^2 \boldsymbol{I})$ // Eq. 5
12 $\boldsymbol{\epsilon}_{t-1}^{(i)} \leftarrow \epsilon_\theta(\mathbf{x}_{t-1}^{(i)}, y)$
13 $\mathbf{x}_{0|t-1}^{(i)} \leftarrow \psi(\mathbf{x}_{t-1}^{(i)}, \boldsymbol{\epsilon}_{t-1}^{(i)})$ // Eq. 4
14 **end**
15 $\mathbf{z} \leftarrow \arg\min_{\mathbf{z}} \sum_{i=1}^{N} \| f_{\mathbf{c}^{(i)}}(\mathbf{z}) - \mathbf{x}_{0|t-1}^{(i)} \|^2$
16 **end**

Algorithm 3: Score Distillation Sampling (SDS)

Inputs: $\mathbf{z}$: A canonical space sample
y: Input text prompt
Outputs: $\mathbf{z}$: Canonical space sample aligned with y

1 **Function** `SDS(z, y)`:
2 **while** $\mathbf{z}$ not converged **do**
3 $t \sim \mathcal{U}(0, T)$; $\mathbf{c} \leftarrow$ `SampleRandomView()`
4 $\mathbf{x}_{0|t} \leftarrow f_{\mathbf{c}}(\mathbf{z})$
// Noise prediction is not used and thus omitted.
5 $\mathbf{x}_{t-1} \sim \mathcal{N}(\mu^*(\mathbf{x}_{0|t}), \sigma_t^2 \boldsymbol{I})$ // Eq. 6
6 $\mathbf{x}_{0|t-1} \leftarrow \psi(\mathbf{x}_{t-1}, \epsilon_\theta(\mathbf{x}_{t-1}, y))$
7 $\mathbf{z} \leftarrow \mathbf{z} - w(t) \left[f_{\mathbf{c}}(\mathbf{z}) - \mathbf{x}_{0|t-1} \right] \frac{\partial f}{\partial \mathbf{z}}$
8 **end**

Algorithm 4: `StochSync`

Inputs: $\mathbf{z}$: A canonical space sample
y: Input text prompt
Outputs: $\mathbf{z}$: Canonical space sample aligned with y

1 **Function** `StochSync(z, y)`:
2 $\mathbf{c}^{1:N} \leftarrow$ `SampleNonOverlappingViews(N)`
$\mathbf{x}_T^{1:N} \sim \mathcal{N}(\mathbf{0}, \boldsymbol{I})$
3 **for** $i = 1 \ldots N$ **do**
4 $\mathbf{x}_{0|T}^{(i)} \leftarrow \mathcal{G}(\mathbf{x}_T^{(i)})$
5 **end**
6 $\mathbf{z} \leftarrow \arg\min_{\mathbf{z}} \sum_{i=1}^{N} \| f_{\mathbf{c}^{(i)}}(\mathbf{z}) - \mathbf{x}_{0|T}^{(i)} \|^2$
7 **for** $t = T \ldots T_{stop} + 1$ **do**
8 $\mathbf{c}^{1:N} \leftarrow$ `SampleNonOverlappingViews(N)` **for** $i = 1 \ldots N$ **do**
9 $\mathbf{x}_{0|t}^{(i)} \leftarrow f_{\mathbf{c}^{(i)}}(\mathbf{z})$
// Noise prediction is not used and thus omitted.
10 $\mathbf{x}_{t-1}^{(i)} \sim \mathcal{N}(\mu^*(\mathbf{x}_{0|t}^{(i)}), \sigma_t^2 \boldsymbol{I})$ // Eq. 6
11 $\mathbf{x}_{0|t-1}^{(i)} \leftarrow \mathcal{G}(\mathbf{x}_{t-1}^{(i)})$
12 **end**
13 $\mathbf{z} \leftarrow \arg\min_{\mathbf{z}} \sum_{i=1}^{N} \| f_{\mathbf{c}^{(i)}}(\mathbf{z}) - \mathbf{x}_{0|t-1}^{(i)} \|^2$
14 **end**

and then projecting it back to each instance space provides the best performance across a broad range of applications. Alg. 2 shows the pseudocode, which, at each step, performs one-step denoising of DDIM for each view (lines 10-11), updates the data point in the canonical space $\mathbf{z}$ while averaging $\mathbf{x}_{0|t}$ by solving a $l2$-minimization (line 13), and then projects $\mathbf{z}$ back to each space (line 9). The differences from the reverse process of DDIM (Alg. 1) are highlighted in blue.

For the stochasticity of the denoising process, typically deterministic DDIM reverse process ($\sigma_t = 0$) (Bar-Tal et al., 2023; Zhang et al., 2024b) or DDPM reverse process ($\sigma_t = \sqrt{(1-\alpha_{t-1})/(1-\alpha_t)}\sqrt{1-\alpha_t/\alpha_{t-1}}$) (Liu et al., 2023) have been used.

Previous works have shown the effectiveness of the synchronization approach in generating various types of visual data using pretrained image diffusion models, including depth-conditioned panoramic images, textures of 3D meshes and Gaussians (Kim et al., 2024a; Liu et al., 2023). However, we have observed that this approach requires strong conditioning for each instance–such as depth images–to achieve optimal quality. In cases where the input condition is not provided, such as generating depth-free 360° panoramas, the outputs tend to show seams as shown in Fig. 2(a), mainly due to the wider data distribution and thus difficulties in achieving convergence during synchronization.

5.2 Score Distillation Sampling

Score Distillation Sampling (SDS) (Poole et al., 2023) and its variants (Wang et al., 2024b; Lukoianov et al., 2024; Liang et al., 2024) are alternatives for generating samples in different spaces. Unlike DS, SDS does not use the reverse diffusion process but instead employs gradient-descent-based updates. The motivation behind SDS is to leverage the loss function from noise predictor training to discriminate real

data points while projecting the canonical data point $f_{\mathbf{c}}(\mathbf{z})$, corrupting it through the forward process, and then predicting the added noise from it.

To clarify the similarities and differences between SDS and DS, we provide a different perspective on understanding SDS, as shown in Alg. 3, aligning each computation with those in DS (Alg. 2). There are several key differences, highlighted as green in Alg. 3. First, the timestep t is not decreased from T to 1 but is randomly sampled until convergence (line 3). Second, while synchronization approaches typically make the reverse process deterministic (Bar-Tal et al., 2023; Zhang et al., 2024b) or identical to DDPM (Liu et al., 2023), SDS uses *maximum stochasticity* ($\sigma_t = \sqrt{1-\alpha_{t-1}}$), thus eliminating the need to maintain the noise ϵ_t. Third, the prediction of the clean sample is updated to the canonical space not by solving the $l2$ minimization but by performing a single gradient descent step (line 7). SDS was originally introduced to perform gradient descent for the loss $\|\boldsymbol{\epsilon} - \epsilon_\theta(\mathbf{x}_{t-1}, y)\|^2$, which is equivalent to the loss used in DS, $\|f_{\mathbf{c}}(\mathbf{z}) - \mathbf{x}_{0|t-1}\|^2$, up to a scale as explained in **Appendix** (Sec. A).

As observed in previous works (Kim et al., 2024a; Huo et al., 2024), when input conditions are provided, the quality of SDS-generated outputs is inferior to that of DS-based methods. However, SDS performs better than DS when no conditions are given (except for the text prompt), effectively integrating images from the instance spaces without producing seams, although it struggles to generate fine details (Fig. 2(b)).

6 StochSync: Stochastic Diffusion Synchronization

Based on our analysis comparing Diffusion Synchronization (DS) and Score Distillation Sampling (SDS) in Sec. 5, we propose our novel method, Stochastic Diffusion Synchronization, or `StochSync` for short, which combines the best features of each method to achieve superior performance in unconditional canonical sample generation. From the perspective of DS, we introduce three key changes in the algorithm.

Maximum Stochasticity in Synchronization. One of the key differences between SDS and previous DS methods is that SDS can be interpreted as utilizing maximum stochasticity in the DDIM denoising step (setting $\sigma_t = \sqrt{1-\alpha_{t-1}}$ in Eq. 5 and thus removing the $\boldsymbol{\epsilon}_t$ term), while earlier DS methods have not explored this aspect. We investigated whether maximum stochasticity helps DS achieve better coherence of samples across instance spaces, similar to what is observed in SDS. As the results shown in Fig. 2(c), it indeed helps remove seams, resulting in much smoother transitions across views. However, we also observe a trade-off between coherence and realism: increased stochasticity leads to greater deviation from the data distribution, producing less realistic images. We present a more detailed analysis of maximum stochasticity on global consistency and realism in **Appendix** (Sec. D), along with experimental results.

Multi-Step $\mathbf{x}_{0|t}$ Computation. To resolve the trade-off between coherence and realism, we propose replacing the computation of $\mathbf{x}_{0|t}$ from Tweedie's formula (Eq. 4), the one-step prediction of the clean sample $\mathbf{x}_0$ from $\mathbf{x}_t$, with a multi-step deterministic denoising process of DDIM, denoted as $\mathcal{G}(\mathbf{x}_t)$. We observe that a more accurate prediction of the clean samples $\mathbf{x}_{0|t}$ at each step along with maximum stochasticity level allows us to achieve both high coherence and realism as shown in Fig. 2(d). Notably, when replacing the computation of $\mathbf{x}_{0|t}$ with multi-step denoising, `StochSync` can also be viewed as iterating SDEdit (Meng et al., 2021): performing the forward process from $\mathbf{x}_{0|t}$ to $\mathbf{x}_{t-1}$ at timestep t (Alg. 4, line 10), followed by the reverse process back to $\mathbf{x}_{0|t-1}$ (line 11). As a result, the loop in line 7 can be interpreted not as performing the reverse process but as iterating SDEdit, meaning it does not need to proceed from timestep T to 1. Empirically, we find that stopping the iteration earlier with $T_{\text{stop}} \gg 1$ provides comparable results while saving computation time. More implementation details and comparisons of inference speed against baseline methods are provided in **Appendix** (Sec. B and Sec. E).

Non-Overlapping View Sampling. In DS, $\mathbf{x}_{0|t}$ is not directly used in the next timestep; instead, it is first averaged in the canonical space (Alg. 2, line 15) and then projected back to the instance space (line 10). We note that this modification of $\mathbf{x}_{0|t}$ also results in a degradation of realism in the final output. To address this, we propose to sample views at each step *without* overlaps. $\mathbf{x}_{0|t}$ is still synchronized *over time*, as the set of non-overlapping views newly sampled at each step has overlaps with the views sampled in previous steps. In practice, we alternate between two sets of non-overlapping views—one being a shift of the other. The result further improved with the non-overlapping views is also shown in Fig. 2(f).

Comparison to DS and SDS. The pseudocode for our `StochSync`, incorporating the aforementioned three major changes from DS, is provided in Alg. 4. Compared to DS (Alg. 2), the $\boldsymbol{\epsilon}_t$ computation is omitted due to the use of maximum stochasticity, Tweedie's formula is changed to a multi-step computation $\mathcal{G}(\cdot)$ (line 11), and the set of views is not fixed but is sampled without overlaps within the set at each step (line 8). In Alg. 4, the changes are highlighted in red. From the SDS perspective, `StochSync` can also be seen as implementing three major changes. First, each iteration is performed not with a random

Table 1: Quantitative results of panorama generation using the prompts provided in PanFusion (Zhang et al. (2024a)). GIQA is scaled by 10^3. The best result in each column is highlighted in **bold**, and the runner-up is underlined.

Method	FID ↓	IS ↑	GIQA ↑	CLIP ↑
SDS	96.44	8.21	17.90	30.87
SDI	143.70	8.08	15.03	29.12
ISM	114.32	8.16	17.08	**31.31**
MVDiffusion	70.49	**10.87**	18.81	30.79
PanFusion	93.85	9.90	17.79	28.21
L-MAGIC	59.83	9.12	19.13	29.73
`StochSync`	**57.88**	10.02	**20.30**	31.01

Table 2: Effectiveness of each components using the prompts provided in PanFusion (Zhang et al. (2024a)). GIQA is scaled by 10^3. The best result in each column is highlighted in **bold**, and the runner-up is underlined.

Id	Max σ_t	Impr. $\mathbf{x}_{0\|t}$	N.O. Views	FID ↓	IS ↑	GIQA ↑	CLIP ↑
1	✗	✗	✗	80.55	8.65	18.22	30.07
2	✔	✗	✗	138.82	6.98	15.68	27.95
3	✗	✔	✗	84.87	7.33	19.06	30.49
4	✔	✔	✗	78.56	8.54	18.44	30.18
5	✔	✗	✔	117.09	7.56	16.32	28.75
6	✔	✔	✔	**57.88**	**10.02**	**20.30**	**31.01**

timestep t but with a linearly decreasing timestep (Alg. 4, line 8), following the scheduling of the reverse process. Second, instead of reflecting $\mathbf{x}_{0|t}$ to the canonical sample $\mathbf{z}$ through gradient descent, we fully minimize the $l2$ loss (line 13). Third, the computation of $\mathbf{x}_{0|t}$ is changed to a multi-step denoising (line 11).

Comparisons to SDS Variants. DreamTime (Huang et al., 2023) suggested decreasing the timestep instead of random sampling. In addition to that, we find that additionally replacing gradient descent with solving a minimization leads to significant improvements. SDI (Lukoianov et al., 2024) takes the opposite approach from ours, reducing the stochasticity of SDS to zero while requiring $\boldsymbol{\epsilon}_t$. Since $\boldsymbol{\epsilon}_t$ cannot be maintained when views are randomly sampled, it is computed by performing DDIM inversion (Mokady et al., 2023) on $\mathbf{x}_{0|t}$ at every timestep. ISM (Liang et al., 2024) also discusses the idea of solving an ODE for $\mathbf{x}_{0|t}$ (multi-step computation) at every timestep, but it does not change gradient descent to solving the minimization.

7 Experiment Results

7.1 360° Panorama Generation

In the 360° panorama generation, the projection operation f is equirectangular projection, which maps a 360° panoramic image to perspective view images. We specifically use 'Stable Diffusion 2.1 Base' as the pretrained diffusion model for all methods, except for the baselines that require finetuned models or inpainting models. We evaluate `StochSync` on sets of prompts provided by the previous works: 121 out-of-distribution prompts from PanFusion (Zhang et al., 2024a) and 20 ChatGPT-generated prompts from L-MAGIC (Cai et al., 2024). The results in the rest of this section are for PanFusion prompts, while the results for L-MAGIC prompts are provided in **Appendix** (Sec. G). For evaluation, we randomly sample 10 perspective view images from each panorama and generate the same number of images using the pretrained diffusion model, which serves as the reference set for the evaluation metrics.

7.1.1 Comparison to Previous Works

Quantitative and qualitative comparisons with the baseline methods using PanFusion (Zhang et al., 2024a) prompts are presented in Tab. 1 and Fig. 3, respectively. For quantitative evaluations, we report FID (Heusel et al., 2018), IS (Salimans et al., 2016), GIQA (Gu et al., 2020), and CLIP score (Radford et al., 2021).

As shown in Tab. 1, `StochSync` outperforms SDS (Poole et al., 2023) and its variants, SDI (Lukoianov et al., 2024) and ISM (Liang et al., 2024), by significant margins in all metrics, except for the CLIP score, where ours is still close to the best. Notably, SDI and ISM are not robust and often generate poor outputs, as examples are shown on the left in rows 2-3 of Fig. 3.

We also compare `StochSync` with finetuning-based methods such as MVDiffusion (Tang et al., 2023) and PanFusion (Zhang et al., 2024a), which finetune a pretrained image diffusion model using panoramic images. Due to the lack of large-scale datasets for panoramic images, these finetuning-based methods tend to overfit to the prompts and images used during training, reducing realism for unseen prompts. Hence, our zero-shot method outperforms these methods quantitatively across all metrics. Qualitatively, our method also demonstrates superior performance compared to theirs, as shown in Fig. 3 (rows 4–5, left).

Lastly, we compare `StochSync` with the state-of-the-art zero-shot 360° panorama generation method, L-MAGIC (Cai et al., 2024), which uses an inpainting diffusion model to sequentially fill a panoramic

images. Quantitatively, StochSync outperforms this method across all metrics. Qualitatively, we observe that L-MAGIC often exhibits a "wavy effect" (Brown & Lowe, 2007) causing the horizon to appear curved, as shown at the bottom left of Fig. 3. For further evaluation, we conducted a user study comparing StochSync and L-MAGIC under various conditions. The details and results of this study are provided in the Appendix (Sec. C).

7.1.2 Ablation Study Results

Tab. 2 and Fig. 3 (right) demonstrate the effectiveness of each component of StochSync discussed in Sec. 6: maximum stochasticity (Max σ_t), multi-step denoising for $\mathbf{x}_{0|t}$ (Impr. $\mathbf{x}_{0|t}$), and non-overlapping view sampling (N.O. Views). As discussed in Sec. 5, DS, represented by SyncTweedies (Kim et al., 2024a), generates plausible local images but lacks global coherence across views and thus produces visible seams (row 1 of Fig. 3). With maximum stochasticity, global coherence improves but at the cost of realism (row 2 of Fig. 3), which is also reflected in the poor quantitative results (row 2 of Tab. 2). Noticeable improvements occur when the computation of $\mathbf{x}_{0|t}$ is also replaced with multi-step denoising, $\mathcal{G}(\mathbf{x}_t)$ (row 4 of Fig. 3 and Tab. 2). Finally, the full version of StochSync, using sets of non-overlapping views, produces the most realistic and coherent panoramic images both qualitatively and quantitatively (row 6 of Fig. 3 and Tab. 2). Refer to the other rows for additional ablation cases.

Metric	Sync-Tweedies	Paint-it	Paint3D	TEXTure	Text2Tex	Sync-Stoch
FID ↓	**21.76**	28.23	31.66	34.98	26.10	<u>22.29</u>
KID ↓	<u>1.46</u>	2.30	5.69	6.83	2.51	**1.31**
CLIP ↑	**28.89**	28.55	28.04	<u>28.63</u>	27.94	28.57

Table 3: Quantitative results of 3D mesh texturing. KID is scaled by 10^3. The best result in each row is highlighted in **bold**, and the runner-up is <u>underlined</u>.

7.2 3D Mesh Texturing

3D mesh texturing is a task where a depth map from each view can be used as a condition for image generation, allowing the use of conditional diffusion models (e.g., ControlNet (Zhang et al., 2023)). While previous DS-based methods perform well when strong conditions are provided, we demonstrate that StochSync, designed to focus on the unconditional case, provides results comparable to previous DS methods and outperforms other state-of-the-art texture generation methods.

In our experiments, we follow the experiment setup of SyncTweedies (Kim et al., 2024a) while using the same 429 mesh and prompt pairs. The quantitative and qualitative results are presented in Tab. 3 and Fig. 4, respectively. Note that the results from other baseline methods are sourced from Kim et al. (2024a). In Tab. 3, StochSync outperforms all other baselines across all metrics, with the exception of SyncTweedies, our base synchronization framework, which shows comparable results. This demonstrates the versatility of our method, as it can be adapted to applications regardless of whether strong conditional inputs are present. In Fig. 4, StochSync generates texture images with fine details, whereas SDS-based and finetuning-based approaches, Paint-it(Youwang et al., 2023) and Paint3D (Zeng et al., 2024), fail to capture these details. Lastly, outpainting-based methods, TEXTure and Text2Tex (Richardson et al., 2023; Chen et al., 2023a), generate texture images with visible seams due to error accumulation.

Fig. 5 also showcases 3D mesh textures on spheres and tori generated by StochSync *without* depth conditioning, showing the potential for various visual content generation (e.g.,game maps).

8 Conclusion and Future Work

We have introduced StochSync, a novel zero-shot method for data generation in arbitrary spaces that fuses Diffusion Synchronization (DS) and Score Distillation Sampling (SDS) into the best form for achieving superior performance in cases where strong conditioning is not provided. Our key insights, based on analyses of the differences between DS and SDS, were to maximize stochasticity in the denoising process to achieve coherence across views, while enhancing realism through multi-step denoising for clean sample predictions at each step and sampling non-overlapping views. We demonstrated state-of-the-art performance in depth-free 360° panorama generation and depth-based mesh texture generation. As a promising direction for future work, we plan to extend our approach by jointly updating both geometry and texture.

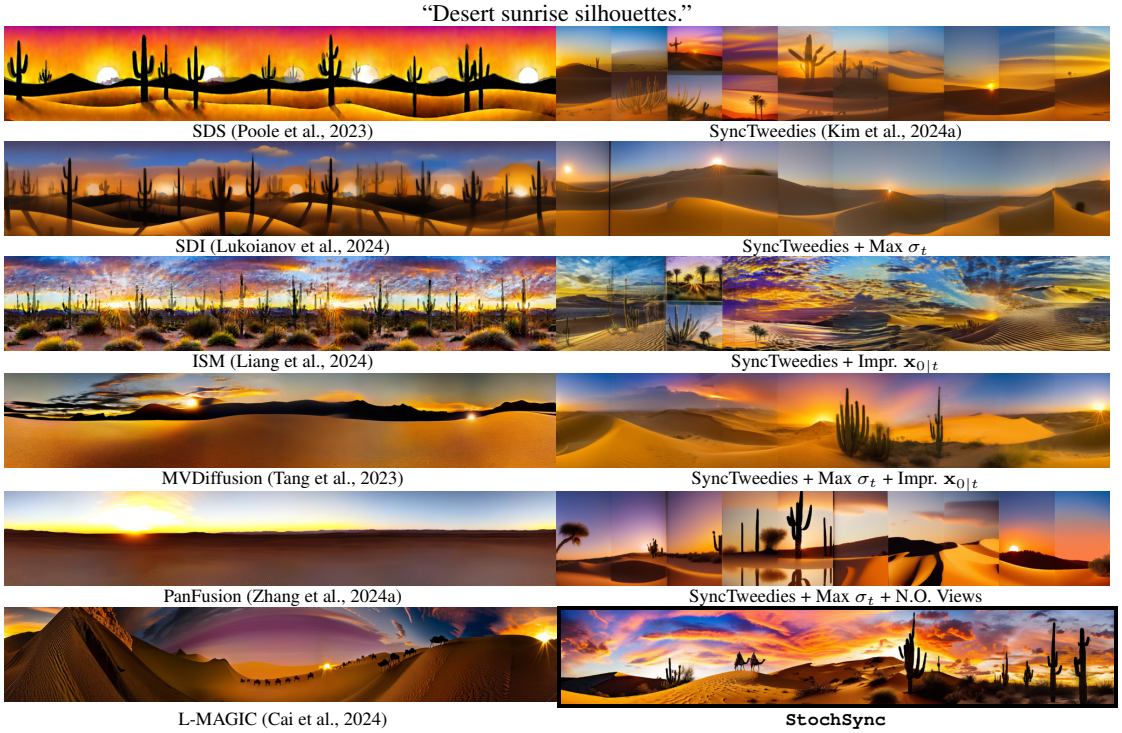

Figure 3: Qualitative results of panorama generation using PanFusion (Zhang et al., 2024a) prompts. Comparisons to previous works are presented in the left column, while the ablation cases are shown in the right column along with `StochSync`.

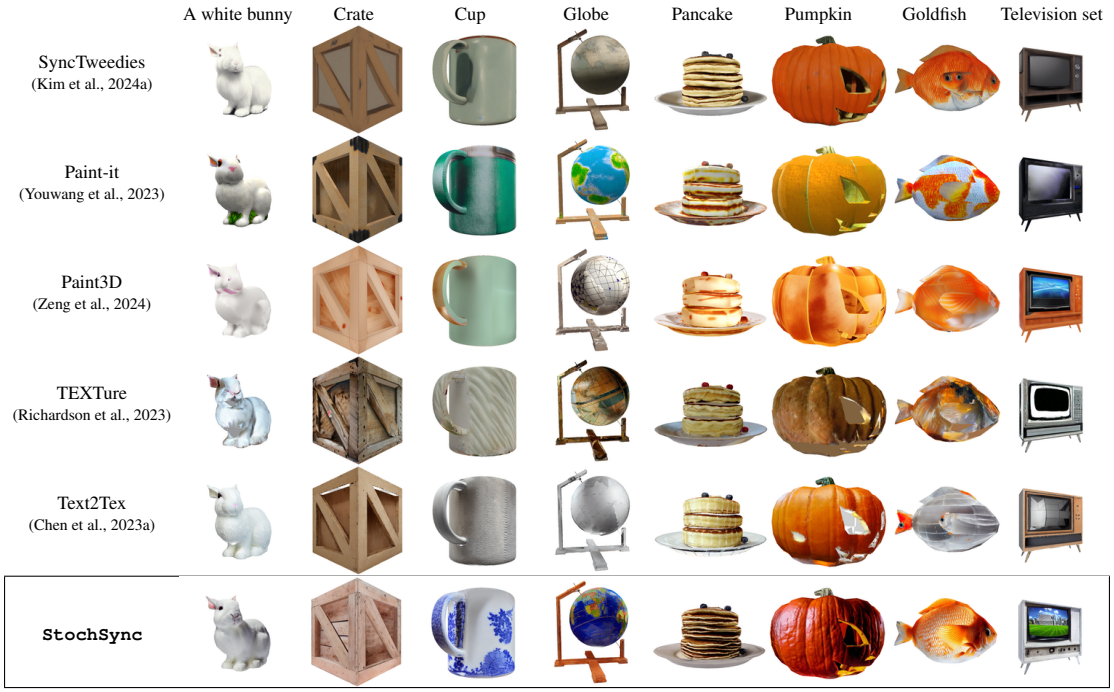

Figure 4: Qualitative result of 3D mesh texturing. `StochSync` generates realistic texture images, demonstrating its applicability even in the conditional generation case.

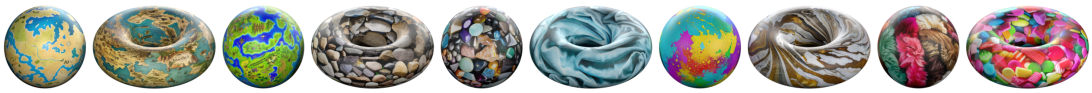

Figure 5: 3D mesh textures on spheres and tori generated by `StochSync`.

ETHICS STATEMENT

`StochSync` leverages a diffusion model (Rombach et al., 2022) trained on the LAION-5B dataset (Schuhmann et al., 2022), which has been preprocessed to remove unethical content. However, despite these efforts, the pretrained diffusion model may still generate undesirable content when presented with misleading or harmful prompts, a limitation that our method also inherits. It is important to acknowledge this risk, as models like `StochSync` could inadvertently produce biased or inappropriate outputs and should be used with caution. Additionally, `StochSync` may impact the creative industry by automating parts of the generative process. However, it also offers opportunities to enhance productivity and accessibility to generative tools.

REPRODUCIBILITY STATEMENT

`StochSync` uses the 'Stable Diffusion 2.1 Base' (Rombach et al., 2022) and the depth-conditioned ControlNet (Zhang et al., 2023), both of which are publicly available. We also provide the pseudocode of `StochSync` in Alg. 4 and the implementation details including hyperparameters in Sec. B. We will also release our code publicly.

REFERENCES

Omer Bar-Tal, Lior Yariv, Yaron Lipman, and Tali Dekel. Multidiffusion: Fusing diffusion paths for controlled image generation. In *ICML*, 2023.

Matthew Brown and David G Lowe. Automatic panoramic image stitching using invariant features. *IJCV*, 2007.

Zhipeng Cai, Matthias Mueller, Reiner Birkl, Diana Wofk, Shao-Yen Tseng, JunDa Cheng, Gabriela Ben-Melech Stan, Vasudev Lai, and Michael Paulitsch. L-magic: Language model assisted generation of images with coherence. In *CVPR*, 2024.

Tianshi Cao, Karsten Kreis, Sanja Fidler, Nicholas Sharp, and Kangxue Yin. Texfusion: Synthesizing 3d textures with text-guided image diffusion models. In *CVPR*, 2023.

Angel Chang, Angela Dai, Thomas Funkhouser, Maciej Halber, Matthias Niessner, Manolis Savva, Shuran Song, Andy Zeng, and Yinda Zhang. Matterport3d: Learning from rgb-d data in indoor environments. In *International Conference on 3D Vision (3DV)*, 2017.

Dave Zhenyu Chen, Yawar Siddiqui, Hsin-Ying Lee, Sergey Tulyakov, and Matthias Nießner. Text2tex: Text-driven texture synthesis via diffusion models. In *ICCV*, 2023a.

Ricky TQ Chen, Yulia Rubanova, Jesse Bettencourt, and David K Duvenaud. Neural ordinary differential equations. *NeurIPS*, 2018.

Rui Chen, Yongwei Chen, Ningxin Jiao, and Kui Jia. Fantasia3D: Disentangling geometry and appearance for high-quality text-to-3d content creation. In *Proceedings of the IEEE/CVF International Conference on Computer Vision*, pp. 22246–22256, 2023b.

Matt Deitke, Dustin Schwenk, Jordi Salvador, Luca Weihs, Oscar Michel, Eli VanderBilt, Ludwig Schmidt, Kiana Ehsani, Aniruddha Kembhavi, and Ali Farhadi. Objaverse: A universe of annotated 3d objects. In *CVPR*, 2023.

Daniel Geng, Inbum Park, and Andrew Owens. Factorized diffusion: Perceptual illusions by noise decomposition. In *ECCV*, 2024a.

Daniel Geng, Inbum Park, and Andrew Owens. Visual anagrams: Generating multi-view optical illusions with diffusion models. In *CVPR*, 2024b.

Shuyang Gu, Jianmin Bao, Dong Chen, and Fang Wen. Giqa: Generated image quality assessment. In *ECCV*, 2020.

Martin Heusel, Hubert Ramsauer, Thomas Unterthiner, Bernhard Nessler, and Sepp Hochreiter. GANs trained by a two time-scale update rule converge to a local nash equilibrium. In *NeurIPS*, 2018.

Jonathan Ho, Ajay Jain, and Pieter Abbeel. Denoising diffusion probabilistic models. In *NeurIPS*, 2020.

Yukun Huang, Jianan Wang, Yukai Shi, Boshi Tang, Xianbiao Qi, and Lei Zhang. Dreamtime: An improved optimization strategy for diffusion-guided 3d generation. In *ICLR*, 2023.

Dong Huo, Zixin Guo, Xinxin Zuo, Zhihao Shi, Juwei Lu, Peng Dai, Songcen Xu, Li Cheng, and Yee-Hong Yang. Texgen: Text-guided 3d texture generation with multi-view sampling and resampling. In *ECCV*, 2024.

Bernhard Kerbl, Georgios Kopanas, Thomas Leimkühler, and George Drettakis. 3d gaussian splatting for real-time radiance field rendering. *ACM TOG*, 2023.

Jaihoon Kim, Juil Koo, Kyeongmin Yeo, and Minhyuk Sung. Synctweedies: A general generative framework based on synchronized diffusions. *arXiv preprint arXiv:2403.14370*, 2024a.

Jeongsol Kim, Geon Yeong Park, and Jong Chul Ye. Dreamsampler: Unifying diffusion sampling and score distillation for image manipulation. In *ECCV*, 2024b.

Yuseung Lee, Kunho Kim, Hyunjin Kim, and Minhyuk Sung. Syncdiffusion: Coherent montage via synchronized joint diffusions. In *NeurIPS*, 2023.

Yixun Liang, Xin Yang, Jiantao Lin, Haodong Li, Xiaogang Xu, and Yingcong Chen. Luciddreamer: Towards high-fidelity text-to-3d generation via interval score matching. In *CVPR*, 2024.

Nan Liu, Shuang Li, Yilun Du, Antonio Torralba, and Joshua B Tenenbaum. Compositional visual generation with composable diffusion models. In *ECCV*, 2022.

Yuxin Liu, Minshan Xie, Hanyuan Liu, and Tien-Tsin Wong. Text-guided texturing by synchronized multi-view diffusion. *arXiv preprint arXiv:2311.12891*, 2023.

Cheng Lu, Yuhao Zhou, Fan Bao, Jianfei Chen, Chongxuan Li, and Jun Zhu. Dpm-solver: A fast ode solver for diffusion probabilistic model sampling in around 10 steps. In *NeurIPS*, 2022a.

Cheng Lu, Yuhao Zhou, Fan Bao, Jianfei Chen, Chongxuan Li, and Jun Zhu. Dpm-solver++: Fast solver for guided sampling of diffusion probabilistic models. *arXiv preprint arXiv:2211.01095*, 2022b.

Andreas Lugmayr, Martin Danelljan, Andres Romero, Fisher Yu, Radu Timofte, and Luc Van Gool. Repaint: Inpainting using denoising diffusion probabilistic models. In *CVPR*, pp. 11461–11471, 2022.

Artem Lukoianov, Haitz Sáez de Ocáriz Borde, Kristjan Greenewald, Vitor Campagnolo Guizilini, Timur Bagautdinov, Vincent Sitzmann, and Justin Solomon. Score distillation via reparametrized ddim. *arXiv preprint arXiv:2405.15891*, 2024.

Chenlin Meng, Yutong He, Yang Song, Jiaming Song, Jiajun Wu, Jun-Yan Zhu, and Stefano Ermon. SDEdit: Guided image synthesis and editing with stochastic differential equations. In *ICLR*, 2021.

Gal Metzer, Elad Richardson, Or Patashnik, Raja Giryes, and Daniel Cohen-Or. Latent-NeRF for shape-guided generation of 3d shapes and textures. In *Proceedings of the IEEE/CVF Conference on Computer Vision and Pattern Recognition*, pp. 12663–12673, 2023.

Ron Mokady, Amir Hertz, Kfir Aberman, Yael Pritch, and Daniel Cohen-Or. Null-text inversion for editing real images using guided diffusion models. In *CVPR*, 2023.

Jangho Park, Gihyun Kwon, and Jong Chul Ye. ED-NeRF: Efficient text-guided editing of 3D scene using latent space NeRF. In *ICLR*, 2023.

Ben Poole, Ajay Jain, Jonathan T. Barron, and Ben Mildenhall. Dreamfusion: Text-to-3D using 2D diffusion. In *ICLR*, 2023.

Alec Radford, Jong Wook Kim, Chris Hallacy, Aditya Ramesh, Gabriel Goh, Sandhini Agarwal, Girish Sastry, Amanda Askell, Pamela Mishkin, Jack Clark, et al. Learning transferable visual models from natural language supervision. In *ICML*, 2021.

Elad Richardson, Gal Metzer, Yuval Alaluf, Raja Giryes, and Daniel Cohen-Or. Texture: Text-guided texturing of 3d shapes. *ACM TOG*, 2023.

Herbert E Robbins. An empirical bayes approach to statistics. In *Breakthroughs in Statistics: Foundations and basic theory*. Springer, 1956.

Robin Rombach, Andreas Blattmann, Dominik Lorenz, Patrick Esser, and Björn Ommer. High-resolution image synthesis with latent diffusion models. In *CVPR*, 2022.

Tim Salimans, Ian Goodfellow, Wojciech Zaremba, Vicki Cheung, Alec Radford, and Xi Chen. Improved techniques for training gans. *NeurIPS*, 2016.

Christoph Schuhmann, Romain Beaumont, Richard Vencu, Cade Gordon, Ross Wightman, Mehdi Cherti, Theo Coombes, Aarush Katta, Clayton Mullis, Mitchell Wortsman, et al. LAION-5B: An open large-scale dataset for training next generation image-text models. In *NeurIPS*, 2022.

Jascha Sohl-Dickstein, Eric Weiss, Niru Maheswaranathan, and Surya Ganguli. Deep unsupervised learning using nonequilibrium thermodynamics. In *ICML*, 2015.

Jiaming Song, Chenlin Meng, and Stefano Ermon. Denoising diffusion implicit models. In *ICLR*, 2021a.

Yang Song, Jascha Sohl-Dickstein, Diederik P Kingma, Abhishek Kumar, Stefano Ermon, and Ben Poole. Score-based generative modeling through stochastic differential equations. In *ICLR*, 2021b.

Shitao Tang, Fuyang Zhang, Jiacheng Chen, Peng Wang, and Yasutaka Furukawa. Mvdiffusion: Enabling holistic multi-view image generation with correspondence-aware diffusion. In *NeurIPS*, 2023.

Xiaojuan Wang, Janne Kontkanen, Brian Curless, Steven M Seitz, Ira Kemelmacher-Shlizerman, Ben Mildenhall, Pratul Srinivasan, Dor Verbin, and Aleksander Holynski. Generative powers of ten. In *CVPR*, 2024a.

Zhengyi Wang, Cheng Lu, Yikai Wang, Fan Bao, Chongxuan Li, Hang Su, and Jun Zhu. Prolificdreamer: High-fidelity and diverse text-to-3d generation with variational score distillation. In *NeurIPS*, 2024b.

Kim Youwang, Tae-Hyun Oh, and Gerard Pons-Moll. Paint-it: Text-to-texture synthesis via deep convolutional texture map optimization and physically-based rendering. *arXiv preprint arXiv:2312.11360*, 2023.

Xianfang Zeng, Xin Chen, Zhongqi Qi, Wen Liu, Zibo Zhao, Zhibin Wang, BIN FU, Yong Liu, and Gang Yu. Paint3d: Paint anything 3d with lighting-less texture diffusion models. In *CVPR*, 2024.

Cheng Zhang, Qianyi Wu, Camilo Cruz Gambardella, Xiaoshui Huang, Dinh Phung, Wanli Ouyang, and Jianfei Cai. Taming stable diffusion for text to 360◦ panorama image generation. In *CVPR*, 2024a.

Hongkun Zhang, Zherong Pan, Congyi Zhang, Lifeng Zhu, and Xifeng Gao. Texpainter: Generative mesh texturing with multi-view consistency. In *SIGGRAPH*, 2024b.

Lvmin Zhang, Anyi Rao, and Maneesh Agrawala. Adding conditional control to text-to-image diffusion models. In *CVPR*, 2023.

APPENDIX

A REFORMULATION OF SDS LOSS

Here, we show that the SDS loss introduced in Sec. 5.2 of the main paper is equivalent to the original loss presented in DreamFusion (Poole et al., 2023) up to a scale. In Sec. 5.2, the SDS loss is presented from the perspective of clean samples:

$$\left\| f_{\mathbf{c}}(\mathbf{z}) - \mathbf{x}_{0|t-1} \right\|^2 = \left\| \frac{\mathbf{x}_{t-1} - \sqrt{1-\alpha_{t-1}}\boldsymbol{\epsilon}}{\sqrt{\alpha_{t-1}}} - \frac{\mathbf{x}_{t-1} - \sqrt{1-\alpha_{t-1}}\epsilon_\theta(\mathbf{x}_{t-1}, y)}{\sqrt{\alpha_{t-1}}} \right\|^2 \tag{7}$$

$$= \frac{1-\alpha_{t-1}}{\alpha_{t-1}} \left\| \boldsymbol{\epsilon} - \epsilon_\theta(\mathbf{x}_{t-1}, y) \right\|^2, \tag{8}$$

where the equality in the first line holds from Eq. 4 and $\boldsymbol{\epsilon}$ is sampled from a standard Gaussian, $\mathcal{N}(\mathbf{0}, \boldsymbol{I})$. Previous works (Kim et al., 2024b; Lukoianov et al., 2024) have also made a similar observation.

B IMPLEMENTATION DETAILS

Panorama Generation. We set the resolution of the perspective view images to 512×512, and the panorama to $2,048 \times 4,096$. A linearly decreasing timestep schedule is employed, starting from $T = 900$ and decreasing to $T_{\text{stop}} = 270$, with a total of 25 denoising steps. For multi-step $\mathbf{x}_{0|t}$ computation, the total number of steps is initially set to 50, decreasing linearly as the denoising process progresses. For view sampling, we alternate between two sets containing five views each, with azimuth angles of $[0°, 72°, 144°, 216°, 288°]$ and $[36°, 108°, 180°, 252°, 324°]$. The elevation angle is set to $0°$, and the field of view (FoV) is set to $72°$.

For methods utilizing multi-step $\mathbf{x}_{0|t}$ predictions, computing $\mathbf{x}_{0|t-1} = \mathcal{G}(\mathbf{x}_{t-1})$ as in line 11 of Alg. 4, only for the last two steps in the loop of line 7, we leverage the previous $\mathbf{x}_{0|t}$ to better preserve the boundary regions. We perform the denoising process while blending the noisy data point as foreground and the previous $\mathbf{x}_{0|t}$ as background, as done in RePaint (Lugmayr et al., 2022). For the background mask, we start from the entire region and gradually decrease the regions over time to be close to the boundaries.

3D Mesh Texturing. For 3D mesh texturing, we follow the approach in SyncTweedies (Kim et al., 2024a) and use the same image and texture resolutions. We use the same number of steps as in the $360°$ panorama generation task with a linearly decreasing time schedule from $T = 1,000$ to $T_{\text{stop}} = 270$. We use 4 views to minimize overlaps between the views. For multi-step $\mathbf{x}_{0|t}$ predictions, we use the same refinement mentioned above.

C USER STUDY DETAILS

In this section, we provide details of the user study described in Sec.7.1.1 of the main paper. We evaluated user preferences across two prompt sets: PanFusion(Zhang et al., 2024a) prompts and a new set of 20 prompts generated by ChatGPT, specifically including the word "horizon." The study was conducted via Amazon Mechanical Turk (AMT).

Screenshots of the user study are shown in Fig.6. Participants were presented with two panoramic images (in random order) generated using the same text prompt: one by L-MAGIC(Cai et al., 2024) and the other by `StochSync`. They were asked to answer the following question: "Which image has better quality, fewer seams, fewer distortions, and better alignment with the given text prompt across the panoramic view?"

Each user study included 25 panoramic images presented in a shuffled order, with five vigilance tests incorporated. For the vigilance tests, participants were shown a wide image composed of concatenated 2D square images alongside a ground truth $360°$ panorama, with the same resolution and question format. To ensure reliability, only responses from participants who passed at least three vigilance tests were considered. In total, we collected responses from 50 out of 96 participants for the PanFusion set and 59 out of 100 participants for the horizon-specific set. Participants were required to be AMT Masters and have an approval rate of over 95%.

Quantitatively, `StochSync` was preferred over L-MAGIC by 56.20% for the PanFusion prompts, with the preference increasing to 64.75% for the horizon-specific prompts, demonstrating `StochSync`'s superior ability to avoid producing curved horizons.

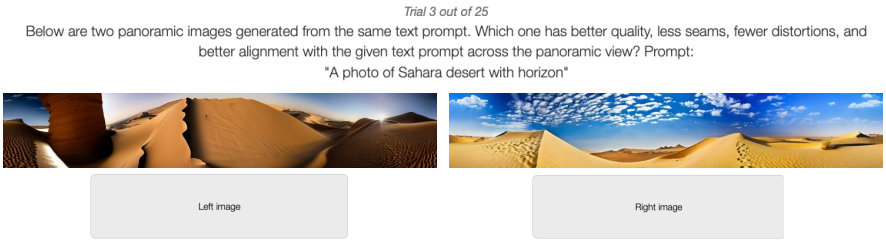

(a) Main problem

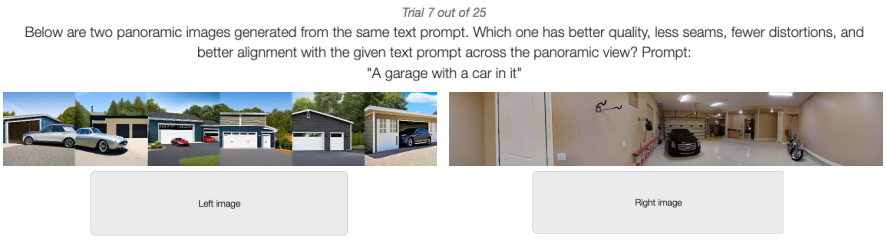

(b) Vigilance test

Figure 6: Screenshots of the user study. The main test is shown in (a), and the vigilance test in (b).

D Analysis of Maximum Stochasticity

D.1 Analysis

Here, we provide an analysis of maximum stochasticity $\sigma_t = \sqrt{1-\alpha_{t-1}}$ in achieving view consistency at the cost of quality degradation. To provide clarity in the analysis, we consider a simplified setup where: (1) the instance space consists of a single image ($N = 1$, line 8, Alg. 4), (2) the projection operation is replaced with an identity function (line 9, Alg. 4), and (3) the objective function is modified to a composition of masked $l2$ losses (lines 6 and 13 of Alg. 4).

Impact of Stochasticity on Consistency. An example of the simplified setup is image inpainting task, where the objective is to generate a realistic image $\mathbf{x}_0$ that aligns with the partial observation $\mathbf{y} = \mathbf{M} \odot \mathbf{x}_0$, where $\mathbf{M} \in \{0, 1\}$ represents a binary mask. To guide the sampling process, the generation is conditioned by replacing $\mathbf{M} \odot \mathbf{x}_{0|t}$ with $\mathbf{y}$.

Under these simplifications, the update rule for $\mathbf{z}$ becomes:

$$\mathbf{z} = \arg\min_{\mathbf{z}} \left[\|(1-\mathbf{M}) \odot (\mathbf{z} - \mathbf{x}_{0|t-1})\|^2 + \|\mathbf{M} \odot (\mathbf{z} - \mathbf{y})\|^2 \right]. \tag{9}$$

To analyze the effectiveness of the level of stochasticity on synchronization, we examine the convergence rate of measurement error, $\mathcal{L}(\mathbf{x}_{0|t}) = \|\mathbf{M} \odot \mathbf{x}_{0|t} - \mathbf{y}\|^2$, for two cases: $\sigma_t = 0$ and $\sigma_t = \sqrt{1-\alpha_{t-1}}$ (Max. σ_t), respectively. As discussed in Sec. 4, when $\sigma_t = 0$, the sampling process becomes fully deterministic. To better illustrate our intuitions, we make two reasonable and straightforward assumptions:

- The initial sample $\mathbf{x}_T \sim \mathcal{N}(\mathbf{0}, \boldsymbol{I})$ satisfies $\mathcal{L}(\mathbf{x}_{0|T}) \gg 0$ and $\mathcal{L}(\mathcal{G}(\mathbf{x}_T)) \gg 0$.
- The pretrained noise prediction network $\epsilon_\theta(\cdot, \cdot)$ is K-Lipschitz, satisfying $|\epsilon_\theta(\mathbf{x}_t, t) - \epsilon_\theta(\mathbf{x}_{t-\Delta t}, t - \Delta t)| < K|\mathbf{x}_t - \mathbf{x}_{t-\Delta t}|$ for some constant K.

Under these assumptions, the reformulation of a one-step denoising process from the perspective of $\mathbf{x}_{0|t}$ yields the following.

$$\mathbf{x}_{0|t-\Delta t} = \mathbf{x}_{0|t} + \sqrt{\frac{1-\alpha_{t-\Delta t}}{\alpha_{t-\Delta t}}} \left(\boldsymbol{\epsilon}_t - \boldsymbol{\epsilon}_{t-\Delta t} \right). \tag{10}$$

$$\therefore |\mathbf{x}_{0|t-\Delta t} - \mathbf{x}_{0|t}| = \sqrt{\frac{1-\alpha_{t-\Delta t}}{\alpha_{t-\Delta t}}} |\boldsymbol{\epsilon}_t - \boldsymbol{\epsilon}_{t-\Delta t}| < \sqrt{\frac{1-\alpha_{t-\Delta t}}{\alpha_{t-\Delta t}}} K |\mathbf{x}_t - \mathbf{x}_{t-\Delta t}| \approx 0, \tag{11}$$

where the approximation equality holds when $\Delta t \approx 0$. This implies that $\mathbf{x}_{0|t-\Delta t}$ is largely dependent by the previous sample $\mathbf{x}_{0|t}$, and as a result, the measurement error $\mathcal{L}(\mathbf{x}_{0|t})$ can remain large even after a few steps of the denoising process, thereby slowing down the convergence of $\mathbf{x}_{0|t}$ to $\mathbf{y}$.

On the other hand, when setting $\sigma_t = \sqrt{1-\alpha_{t-1}}$ (Max. σ_t), $\mathbf{x}_{0|t-\Delta t}$ is no longer dependent on $\mathbf{x}_{0|t}$, allowing $\mathbf{x}_t$ and $\mathbf{x}_{t-\Delta t}$ to differ significantly, even for small Δt.

This process can be interpreted as *resetting* the denoising trajectory based on $\mathbf{x}_{0|t}$, allowing the exploration of $\mathbf{x}_{t-\Delta t}$ that minimizes the measurement error. While it is also true that the newly sampled $\mathbf{x}_{t-\Delta t}$ could potentially deviate from the desired trajectory and increase $\mathcal{L}(\mathbf{x}_{0|t-\Delta t})$, our empirical observations show that, in most cases, it converges to the measurement within a few denoising steps.

Impact of Stochasticity on Quality. However, we also observed that sampling with Max. σ_t degrades the quality of the sample $\mathbf{x}_0$. To address this, we examine the process of sampling $\mathbf{x}_{t-\Delta t}$ using Max. σ_t, which is described as $\mathbf{x}_{t-\Delta t} = \sqrt{\alpha_t}\mathbf{x}_{0|t} + \sqrt{1-\alpha_t}\boldsymbol{\epsilon}$, where $\boldsymbol{\epsilon} \sim \mathcal{N}(\mathbf{0}, \boldsymbol{I})$.

Note that this equation is equivalent to the forward diffusion process described in Eq. 2 except the approximation of $\mathbf{x}_0$ to $\mathbf{x}_{0|t}$. Unfortunately, as the one-step prediction $\mathbf{x}_{0|t}$ computed using Tweedie's formula (Robbins, 1956) often deviate from the clean data manifold, sampling process using Max. σ_t leads to $\mathbf{x}_{t-\Delta t}$ being placed in low-density regions of the noisy data distribution, ultimately degrading the quality of $\mathbf{x}_0$. Inspired by this observation, we note that $\mathbf{x}_{0|t}$ should be well-aligned with the clean data $\mathbf{x}_0$ to ensure $\mathbf{x}_{0|t-\Delta t}$ to be placed in high-density regions.

This motivates us to incorporate Impr. $\mathbf{x}_{0|t}$, which replaces the one-step predicted $\mathbf{x}_{0|t}$ with a more realistic, multi-step predicted $\mathbf{x}_{0|t}$. Additionally, averaging multiple $\mathbf{x}_{0|t}$ can introduce blurriness, potentially causing the sample to deviate from the clean data manifold, which leads to the adoption of N.O. Views.

Effect of Increasing the Number of Steps. One might question the validity of Impr. $\mathbf{x}_{0|t}$ compared to using a larger number of steps, as suggested in DDIM (Song et al., 2021a), which demonstrates that increasing the number of sampling steps can improve the quality of generated samples when stochasticity is introduced. However, it is important to note that this claim does not apply to our method, as the DDIM framework focuses on cases where the level of stochasticity falls within the range of $\sigma_t = 0$ to $\sigma_t = \sqrt{\frac{1-\alpha_{t-1}}{1-\alpha_t}\left(1-\frac{\alpha_t}{\alpha_{t-1}}\right)}$ (DDPM).

`StochSync` sets $\sigma_t = \sqrt{1-\alpha_{t-1}}$, utilizing the maximum level of stochasticity. Under this setting, the trend observed in DDIM no longer applies. Specifically, increasing the number of sampling steps does not consistently lead to improved generation quality. In the following, we present an informal proof to explain the underlying reason for this divergence.

Statement. Under maximum stochasticity, the diffusion forward process diverges and cannot be approximated by a Stochastic Differential Equation (SDE) as the timestep interval approaches zero.

Proof. Consider the generalized forward diffusion process proposed in DDIM (Song et al., 2021a):

$$\begin{aligned}\mathbf{x}_{t+\Delta t} = &\left(\sqrt{\alpha_{t+\Delta t}} - \frac{\sqrt{1-\alpha_{t+\Delta t}}\sqrt{\alpha_t}}{1-\alpha_t}\sqrt{1-\alpha_t-\sigma_{t+\Delta t}^2}\right)\mathbf{x}_{0|t} \\ &+ \frac{\sqrt{1-\alpha_{t+\Delta t}}\sqrt{1-\alpha_t-\sigma_{t+\Delta t}^2}}{1-\alpha_t}\mathbf{x}_t \\ &+ \sqrt{\frac{1-\alpha_{t+\Delta t}}{1-\alpha_t}}\sigma_{t+\Delta t}\boldsymbol{\epsilon},\end{aligned} \tag{12}$$

where $\boldsymbol{\epsilon} \sim \mathcal{N}(\mathbf{0}, \boldsymbol{I})$. For this process to converge to a SDE as $\Delta t \to 0$, Lipschitz continuity requires both sides of the equation to approach $\mathbf{x}_t$. A necessary condition for this is $\lim_{\Delta t \to 0} \sigma_t = 0$. However, under the maximum level of stochasticity, where $\sigma_t = \sqrt{1-\alpha_{t-1}}$, this condition is violated. Consequently, increasing the number of timesteps does not refine the distribution but instead causes it to deviate further, leading to lower-quality or unrealistic images. □

D.2 EXPERIMENTS

Experiment 1: Image Inpainting. Qualitative results of image inpainting using $\sigma_t = 0$, Max. σ_t, and `StochSync` are presented in Fig. 7 and Fig. 8. The images are obtained by solving the ODE, $\mathcal{G}(\mathbf{x}_t)$, initialized from the same random noise $\mathbf{x}_T$. Red boxes are used to highlight the convergence of $\mathbf{x}_{0|t}$ to $\mathbf{y}$. As illustrated, methods with maximum stochasticity (Max. σ_t and `StochSync`) converge significantly faster than $\sigma_t = 0$, a trend also reflected in the measurement error plot (Fig. 9). Additionally, `StochSync` improves Max. σ_t by mitigating quality degradation in unobserved regions.

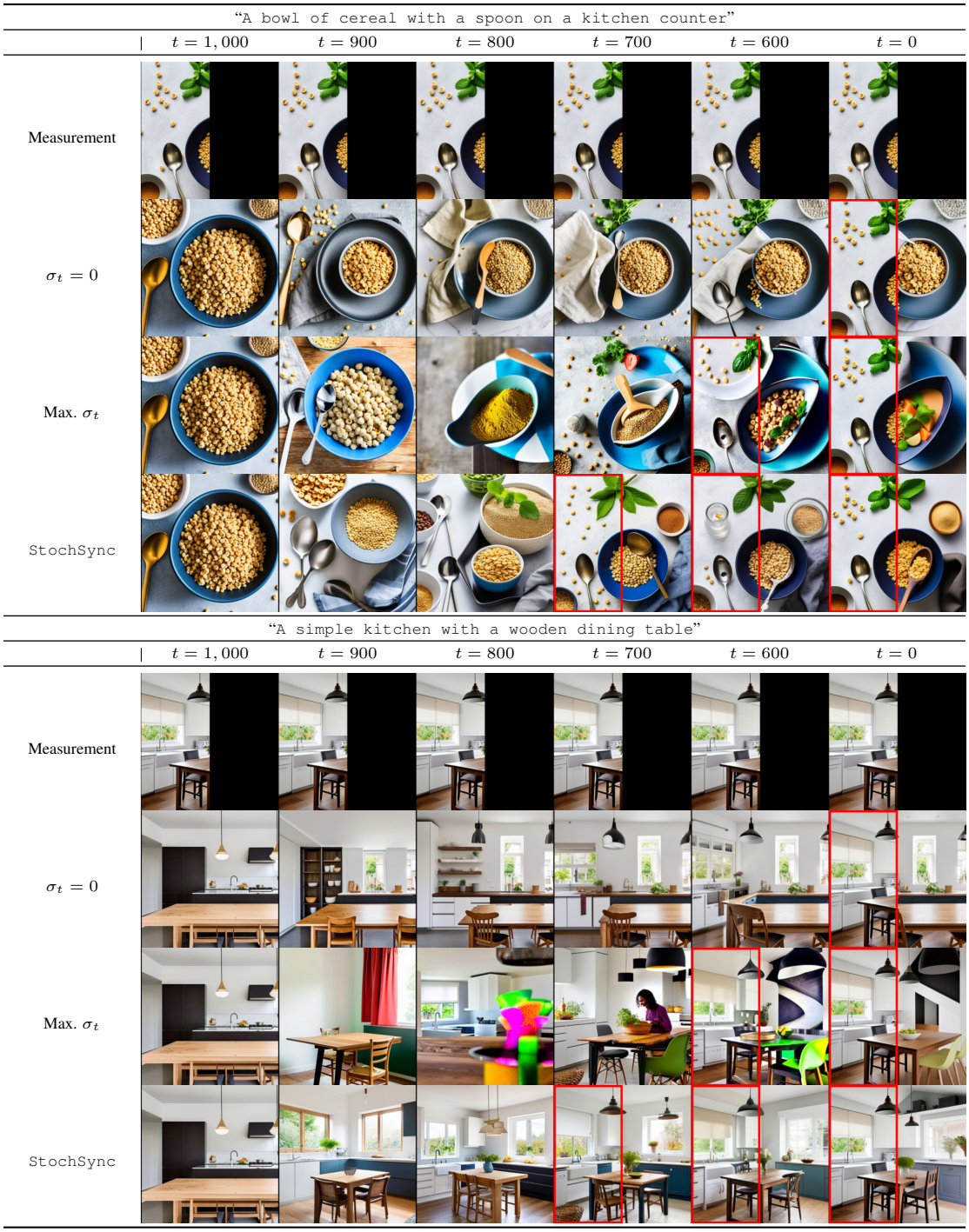

Figure 7: Qualitative result of image inpainting.

Figure 8: Qualitative results of image inpainting.

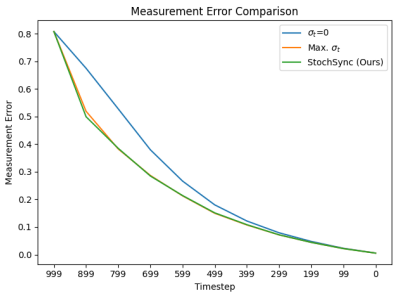

Figure 9: Measurement error plotted against denoising timesteps. For $\sigma_t = 0$, the error remains larger than for cases with maximum stochasticity (Max. σ_t and StochSync).

"A DSLR photo of a dog"

Number of Steps $= 10$	Number of Steps $= 100$	Number of Steps $= 1,000$	Number of Steps $= 10,000$

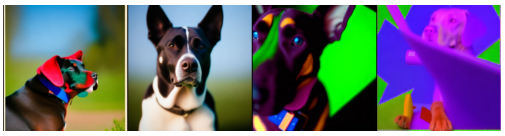

Figure 10: Qualitative results of image generation with Max. σ_t. Each image is obtained by running different numbers of steps. Sampling images with Max. σ_t for a large number of steps fails to generate plausible images.

Experiment 2: Effect of Increasing the Number of Steps. To validate the theoretical insight on maximum stochasticity diverging for large timesteps, we conduct experiments on image generation under maximum stochasticity with varying number of timesteps. We present qualitative results in Fig. 10, which demonstrate that increasing the number of timesteps eventually results in unrealistic images.

E Inference Time Comparison

A potential concern about StochSync could be its computational efficiency, particularly the multi-step computation of $\mathbf{x}_{0|t}$, which might seem to introduce significant overhead. However, we show that this is not the case as our method with optimized hyperparameters achieves a runtime comparable to L-MAGIC Cai et al. (2024) and even outperforms MVDiffusion Tang et al. (2023). Notably, when integrated with a more efficient ODE solver, our method achieves the fastest runtime for 360° panorama generation, highlighting its computational efficiency.

Experiment Setup. Since StochSync can be interpreted as an iterative application of SDEdit Meng et al. (2021) across views, the denoising process does not need to run fully to $t = 0$. Instead, it can stop at $t = T_{\text{stop}} \gg 0$, effectively reducing the number of denoising steps. The optimal configuration was found to be $T_{\text{stop}} = 700$ with 8 denoising steps, which we denote as StochSync*.

Further improvements in efficiency were achieved by incorporating advanced ODE solvers, such as DPM-Solver (DPM-S) Lu et al. (2022a;b). This integration, referred to as StochSync* + DPM-S, enables efficient computation of multi-step $\mathbf{x}_{0|t}$ with fewer ODE steps, reducing the total from 50 to 20 while maintaining comparable output quality.

Experiment Results. In Tab. 4 and Tab. 5, we present a runtime comparison of StochSync with the baselines for 360° panorama generation and 3D mesh texturing, respectively. For the runtime comparison, the vanilla StochSync was evaluated using the setup described in 7, while baseline methods were tested with their default parameters: 50 denoising steps for MVDiffusion (Tang et al., 2023) and PanFusion (Zhang et al., 2024a), 30 steps for SyncTweedies (Kim et al., 2024a), and 25 steps for L-MAGIC (Cai et al., 2024). For 3D mesh texturing, the running time results are sourced from SyncTweedies (Kim et al., 2024a).

As shown in Tab. 4, StochSync* achieves a runtime comparable to the baselines in 360° panorama generation thanks to early stopping. When combined with DPM-Solver (Lu et al., 2022b) (StochSync+DPM-S), as noted in Tab. 4 and Tab. 5, the computation becomes even faster with only a small amount of quality loss. For instance, in 360° panoramas, **StochSync** achieves FID/IS/GIQA/CLIP scores of 57.88/10.02/20.30/31.01, while **StochSync*** and **StochSync**+DPM-S obtain 47.24/10.80/21.41/31.07 and 47.59/10.43/21.27/31.03, respectively. Similarly, for mesh texturing, the FID/KID/CLIP scores change only slightly—from 22.29/1.31/28.57 for **StochSync** to 25.22/2.41/28.60 for **StochSync**+DPM-S.

Table 4: Quantitative results of panorama generation using the out-of-distribution prompts provided in PanFusion (Zhang et al. (2024a)). The best result in each column is highlighted in **bold**, and the runner-up is underlined.

Method	Runtime (seconds) ↓
SyncTweedies	46.84
SDS	>1K
SDI	920.49
ISM	>1K
MVDiffusion	75.57
PanFusion	38.33
L-MAGIC	58.59
StochSync	149.32
StochSync*	57.80
StochSync* +DPM-S	**28.05**

Table 5: Quantitative results of 3D mesh texturing. The best result in each column is highlighted in **bold**, and the runner-up is underlined.

Method	Runtime (minutes) ↓
SyncTweedies	1.83
Paint-it	21.95
Paint3D	2.65
TEXTure	**1.54**
Text2Tex	13.10
StochSync	7.61
StochSync+DPM-S.	3.36

F Additional Applications

In this section, we provide qualitative results of additional applications of StochSync including high resolution panorama generation (Fig. 11) and texturing 3D Gaussians (Kerbl et al., 2023) (Fig. 12).

High Resolution Panorama Generation. To extend StochSync to high-resolution panorama generation, we modify the original panorama generation setup by narrowing the field of view for individual views and increasing the number of samples, resulting in a higher-resolution canonical space sample. However, increasing the number of views introduces the risk of repetitive objects appearing in the scene. To mitigate this, we employed the refinement technique inspired by SDEdit Meng et al. (2021). Specifically, the panorama is first generated using the original setup described in Sec. B. The resulting image is perturbed with noise to a specific timestep and then refined through the sampling process restarted from this point. This approach effectively addresses repetitive patterns while maintaining high-fidelity details. The qualitative results of 8K panorama generation are presented in Fig. 11, demonstrating sharp and visually consistent outputs.

3D Gaussians Texturing We further demonstrate the capability of StochSync in applications involving complex non-linear projection operations through texturing 3D Gaussians Kerbl et al. (2023). In this experiment, we used Gaussians reconstructed from the Synthetic NeRF dataset Park et al. (2023), updating only their color parameters while keeping their positions and covariances fixed. The results, shown in Fig. 12, demonstrate that StochSync can successfully generate textures of 3D Gaussians.

"Quirky steampunk workshop filled with gears and gadgets"

StochSync

StochSync w/ 8K Res.

"Rocky desert landscape with towering saguaro cacti"

StochSync

StochSync w/ 8K Res.

"Elegant ballroom with crystal chandeliers and marble floors"

StochSync

StochSync w/ 8K Res.

Figure 11: Qualitative results of high resolution panorama generation using StochSync.

Figure 12: Qualitative results of texturing 3D Gaussians (Kerbl et al., 2023) using `StochSync`.

Table 6: Quantitative results of panorama generation using the prompts provided in L-MAGIC (Cai et al. (2024)). GIQA is scaled by 10^3. The best result in each column is highlighted in **bold**, and the runner-up is underlined.

Method	FID ↓	IS ↑	GIQA ↑	CLIP ↑
SDS	163.23	5.60	17.41	30.37
SDI	171.69	5.93	16.42	29.33
ISM	197.10	4.92	16.52	29.44
MVDiffusion	111.12	6.17	**20.71**	31.07
PanFusion	151.60	5.48	18.19	28.46
L-MAGIC	112.72	5.94	19.73	30.39
`StochSync`	**109.41**	**6.20**	20.31	**31.22**

Table 7: Effectiveness of each components using the prompts provided in L-MAGIC (Cai et al. (2024)). GIQA is scaled by 10^3. The best result in each column is highlighted in **bold**, and the runner-up is underlined.

Id	Max σ_t	Impr. $\mathbf{x}_{0\|t}$	N.O. Views	FID ↓	IS ↑	GIQA ↑	CLIP ↑
1	✗	✗	✗	120.19	5.58	19.68	29.34
2	✔	✗	✗	178.03	4.76	17.43	28.02
3	✗	✔	✗	139.34	4.83	18.94	30.08
4	✔	✔	✗	126.58	5.41	19.34	30.04
5	✔	✗	✔	169.32	4.74	16.67	28.53
6	✔	✔	✔	**109.41**	**6.20**	**20.31**	**31.22**

G Additional Results

Quantitative Results of $360°$ Panorama Generation Using L-MAGIC Prompts. The quantitative results of panorama generation using the prompts from L-MAGIC (Cai et al., 2024), as well as the ablation study results, are presented in Tab. 6 and Tab. 7, respectively. We observe the same trend as discussed in Sec. 7.1, where the results with PanFusion (Zhang et al., 2024a) prompts are discussed. `StochSync` generates high-fidelity panoramic images, while L-MAGIC tends to produce panoramas with curved horizons. Refer to Sec. G.2 for qualitative results.

Additional Results of $360°$ Panorama Generation Using Horizon Prompts. Qualitative comparisons of `StochSync` and L-MAGIC (Cai et al., 2024) on the horizon-specific prompt set discussed in Sec. 7.1.1 are shown in Fig. 13. As discussed in Sec. 7.1.1, L-MAGIC tends to generate wavy panoramas with global distortions, while `StochSync` produces more realistic panoramic images. This aligns with the results of the user preference test presented in Sec. 7.1.1, where `StochSync` outperforms L-MAGIC on both the PanFusion and horizon-specific prompts.

Additional Results of 3D Mesh Texturing. Extending the qualitative results presented in Fig. 4, we provide more qualitative results of 3D mesh texturing in Fig. 14.

Figure 13: Qualitative comparisons between L-MAGIC (Cai et al., 2024) and `StochSync` on the horizon-specific prompts.

Figure 14: Additional qualitative results of 3D mesh texturing.

More qualitative results of 360° panorama generation are presented in the following pages.

G.1 Additional 360° Panorama Generation Results Using PanFusion Prompts

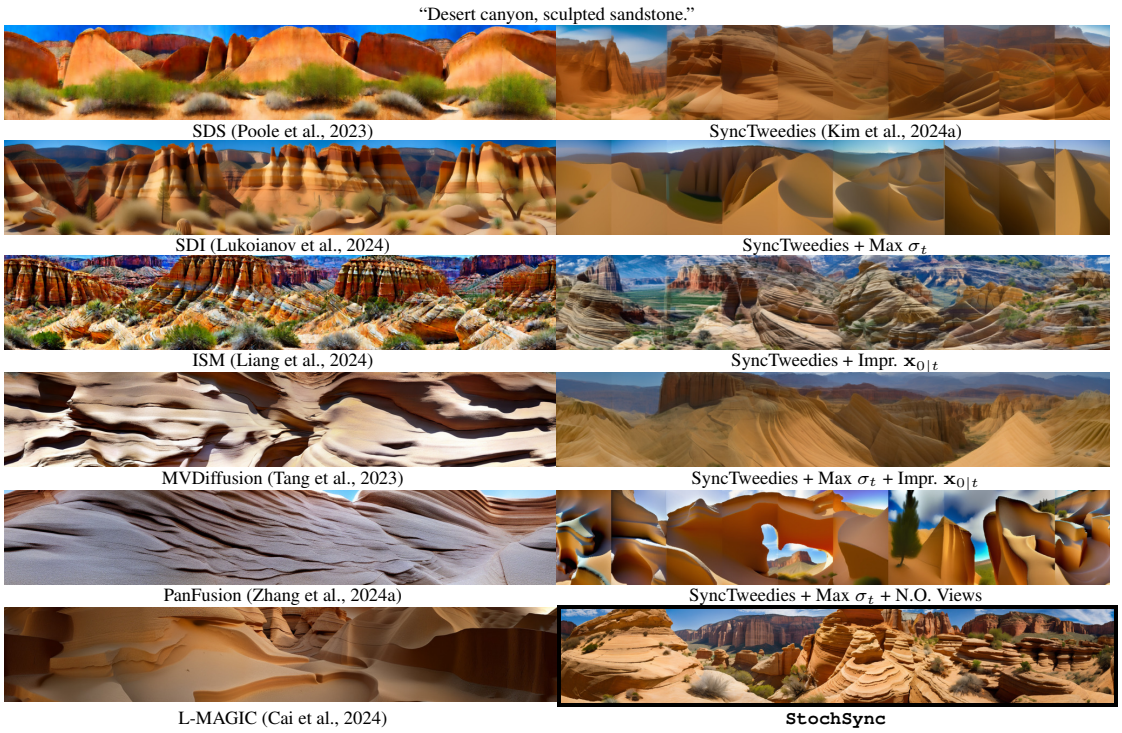

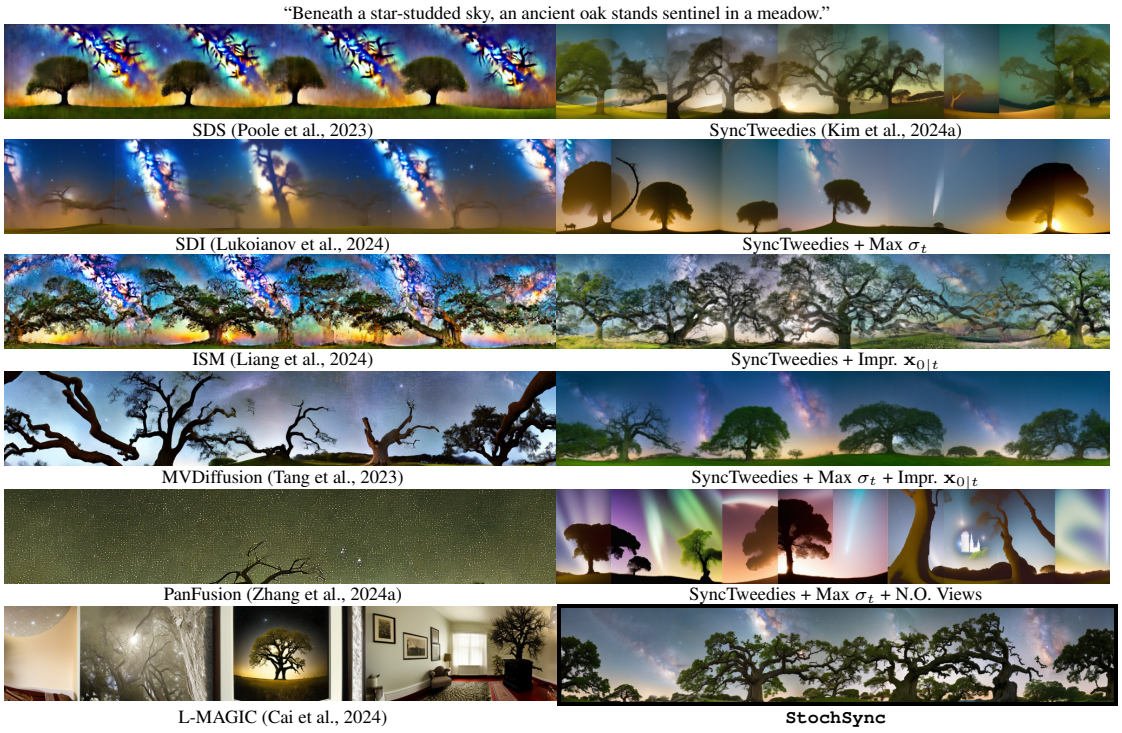

"Desert dunes, endless golden waves."

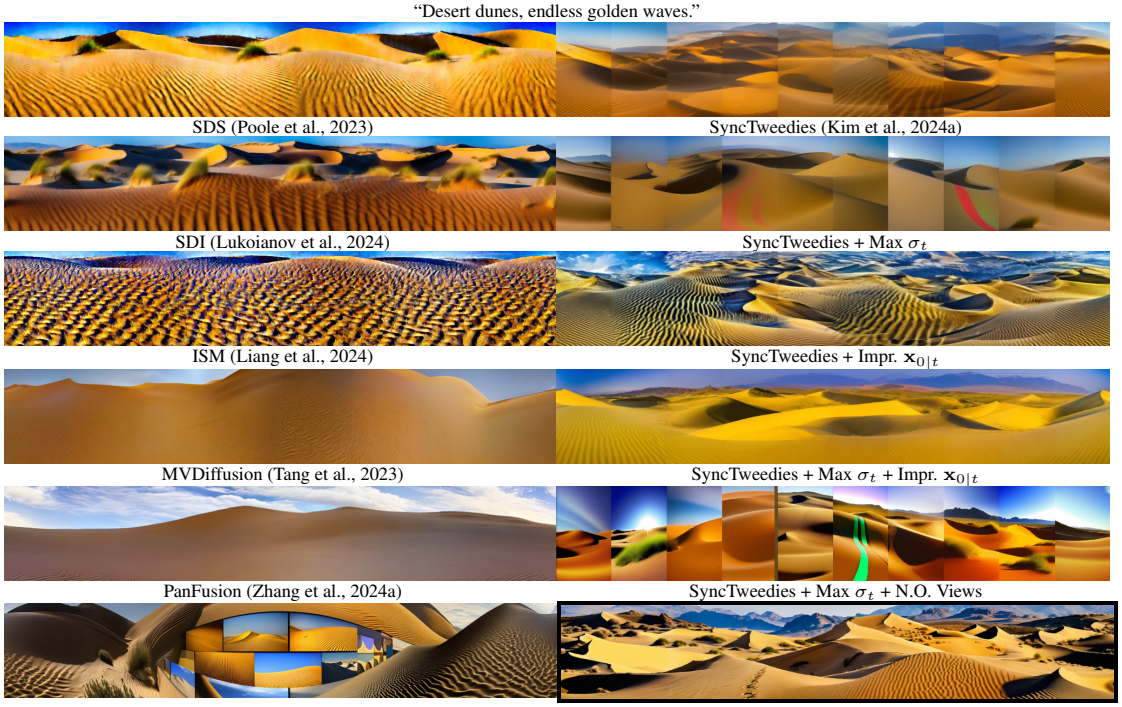

"Redwood forest, towering tranquility."

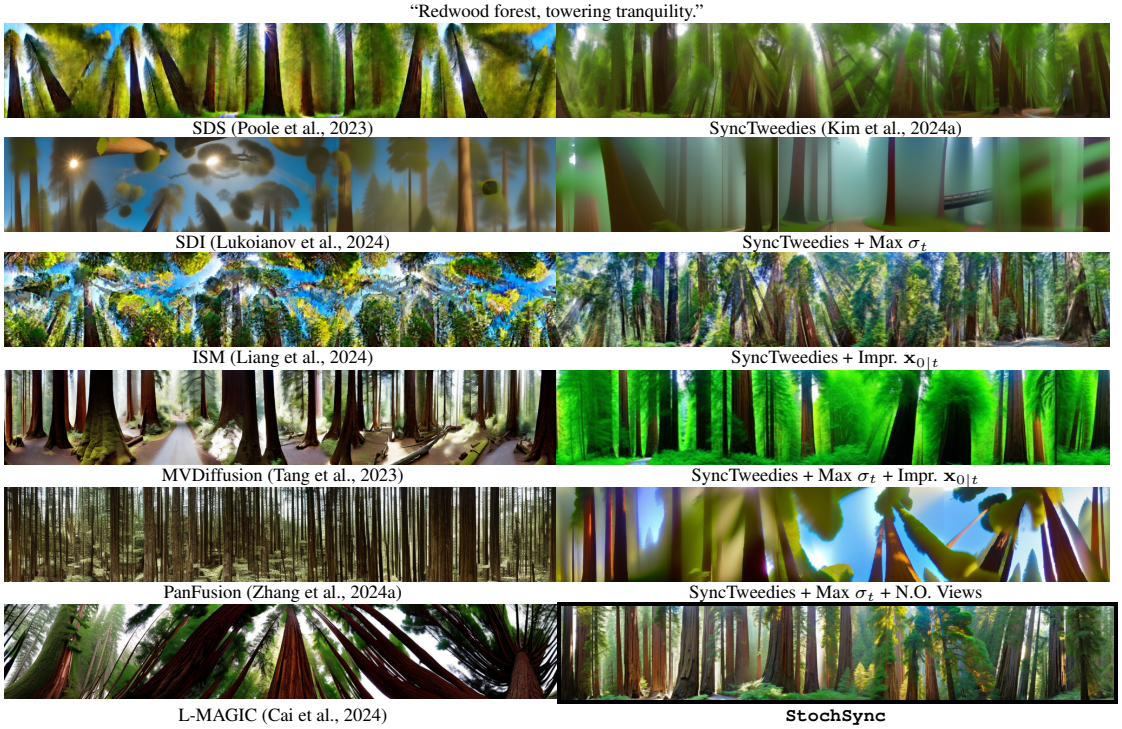

"Moonlit beach, waves whispering secrets."

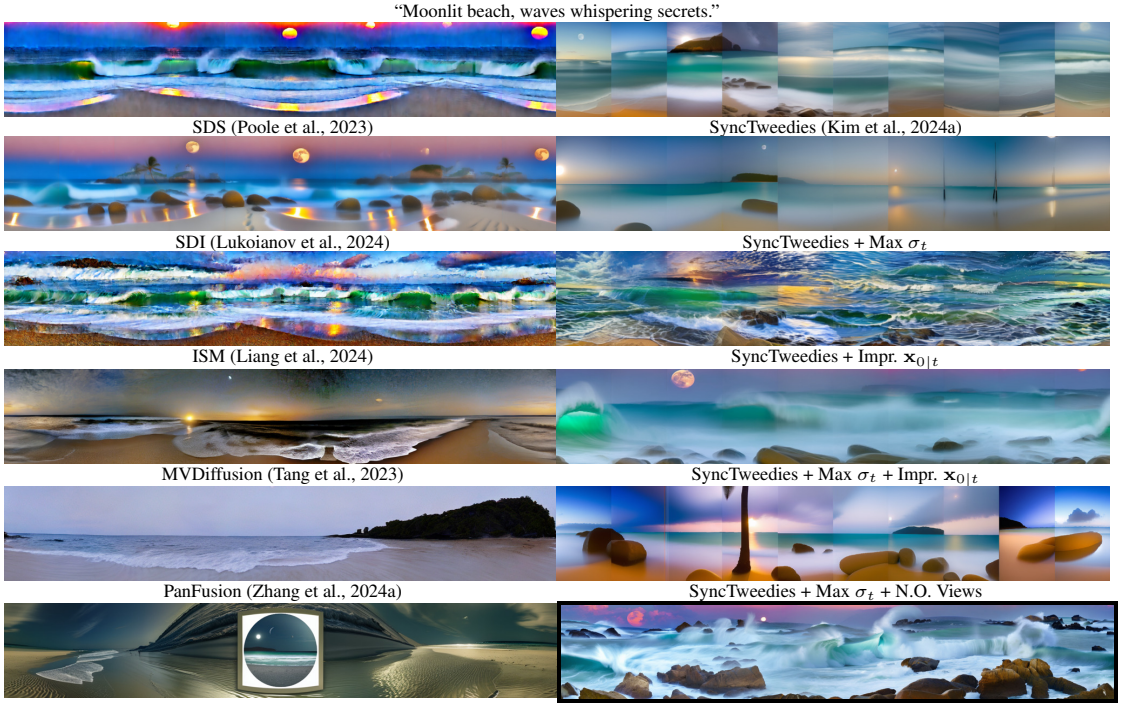

"On a distant planet surface, towering crystalline structures rise against an alien sky."

"Nestled in a canyon, a pueblo village stands against the red earth."

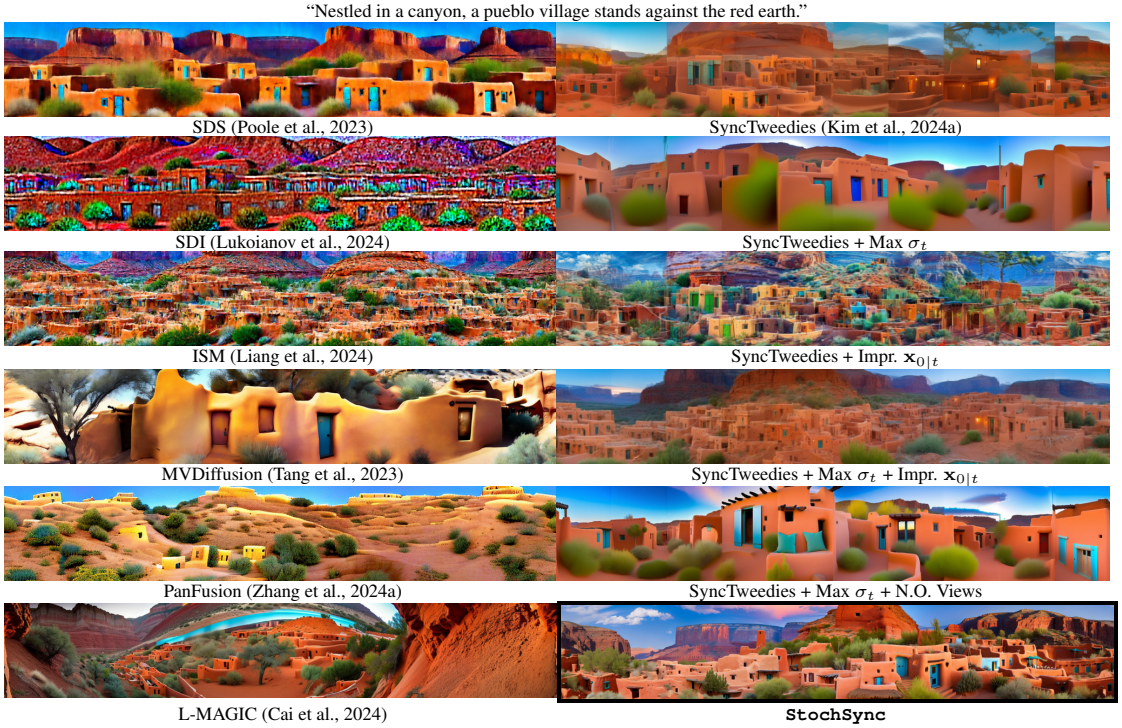

"On the surface of a distant planet, a landscape of alien rock formations and swirling, multicolored gases."

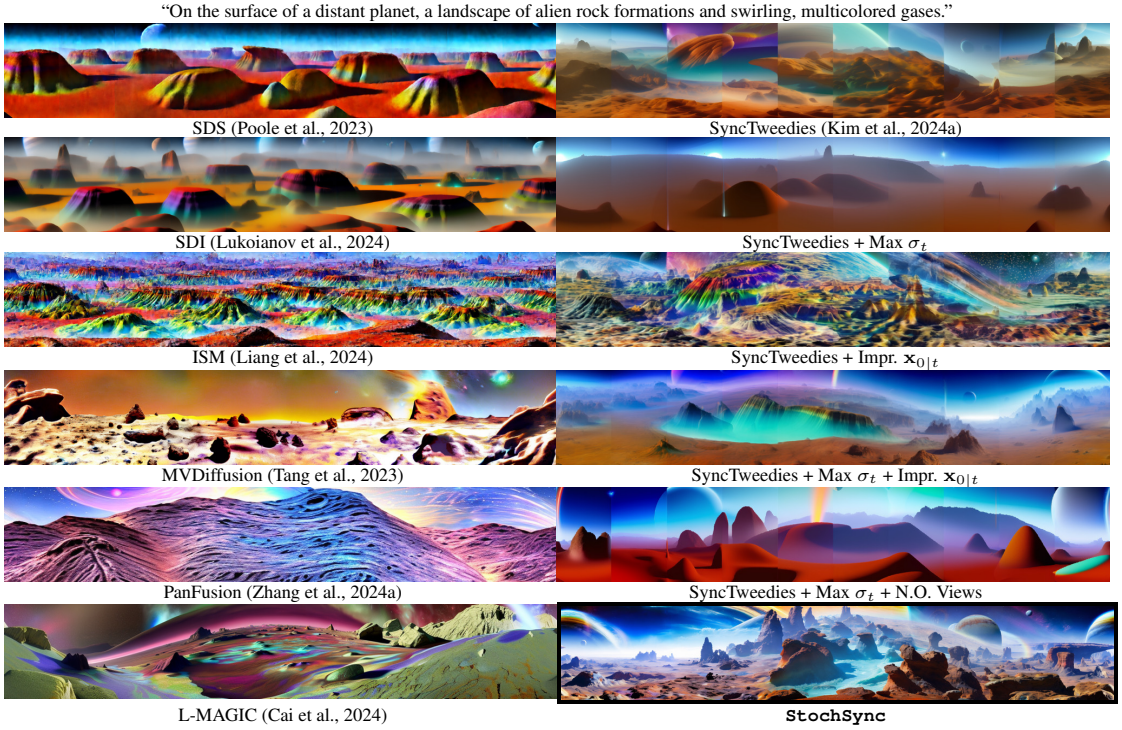

"The interior of a historic library, filled with rows of antique books, leather-bound and dust-covered."

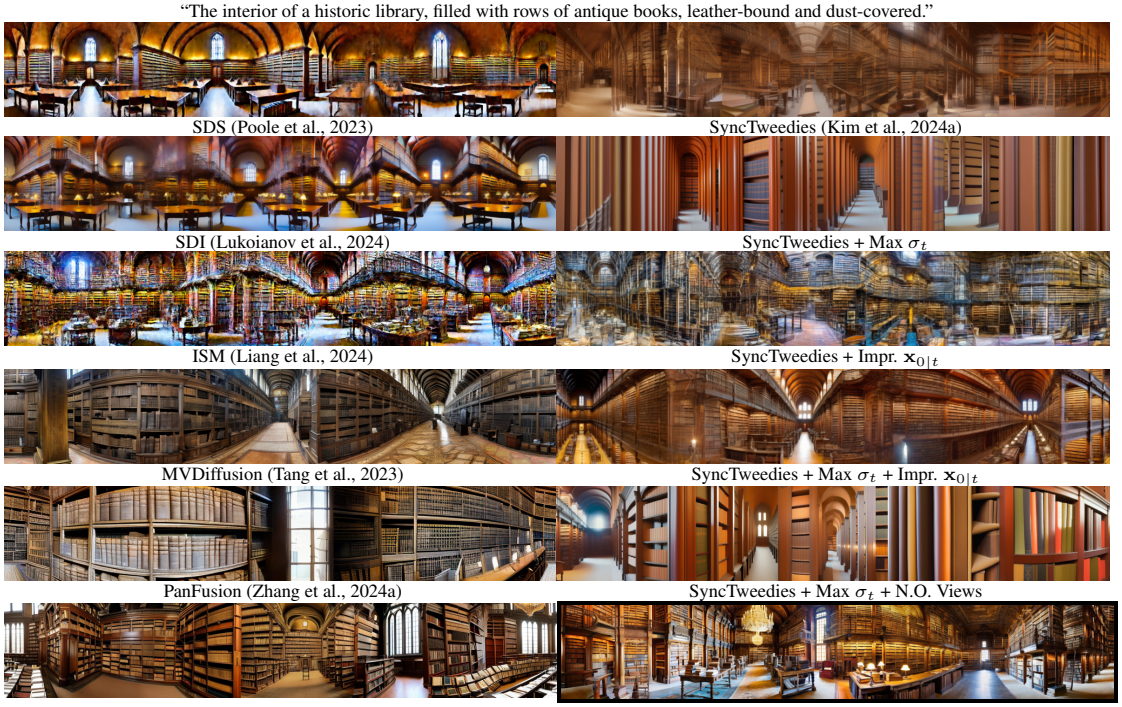

"Hidden waterfall, cascading down moss-covered rocks in a tranquil glade."

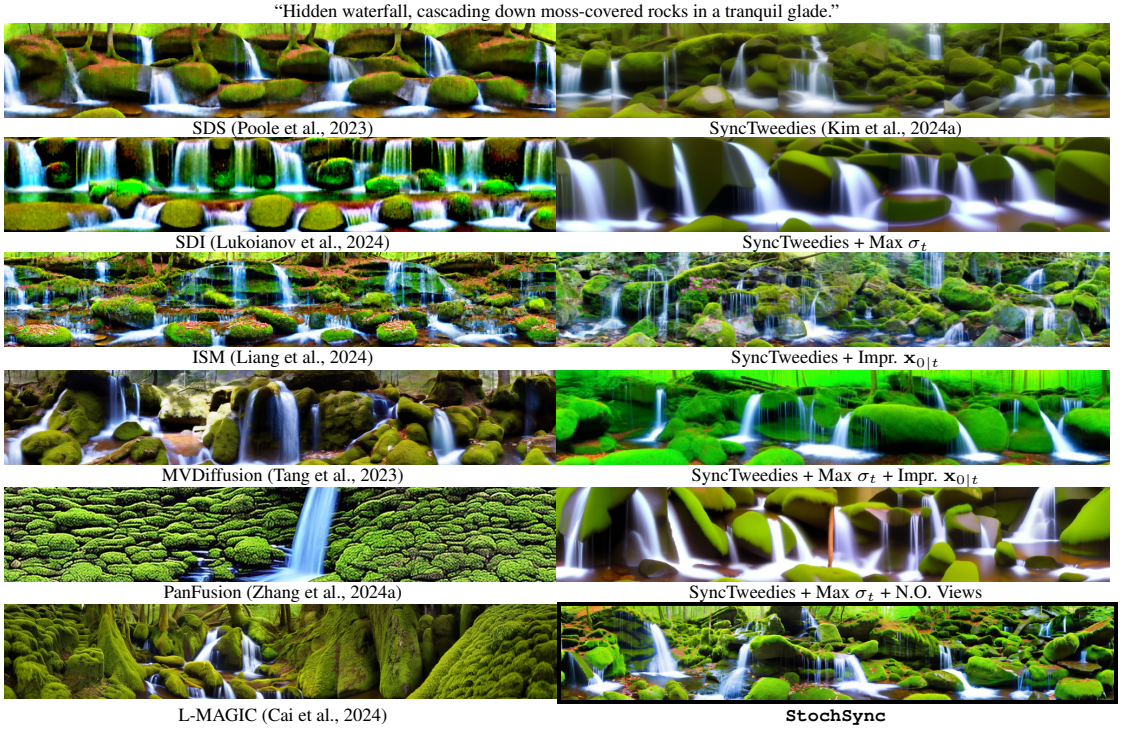

"Surreal desert, mirage of shimmering heat, dunes stretching endlessly."

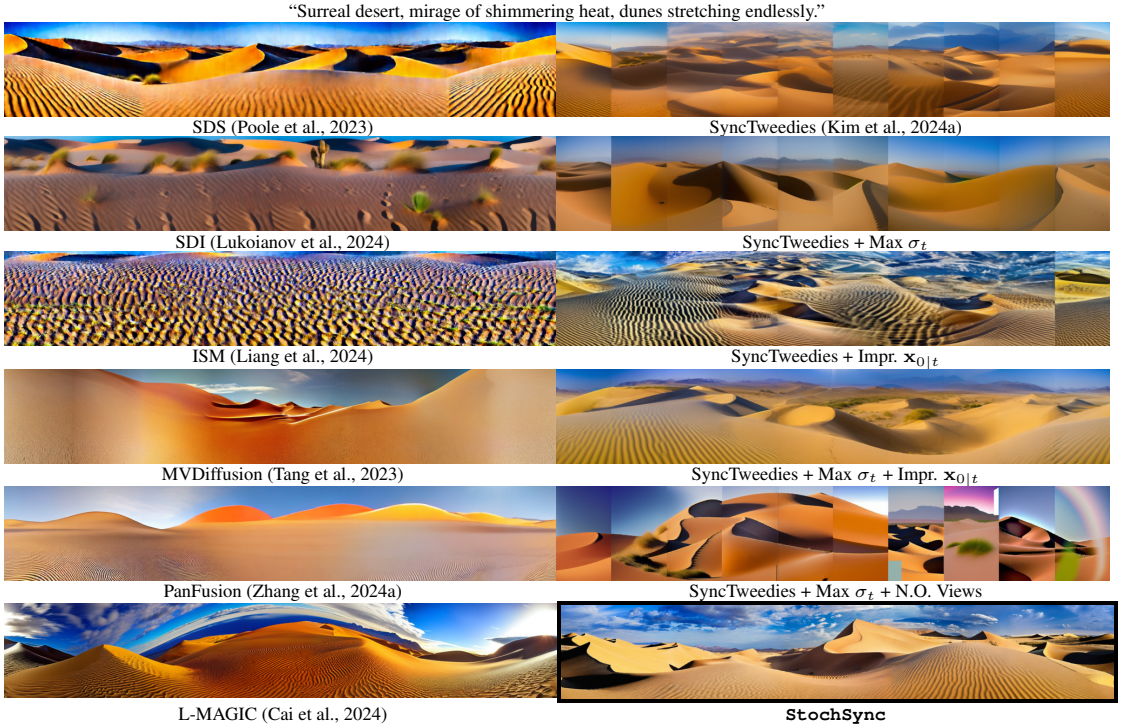

"Alpine meadow, wildflowers swaying in a mountain breeze, snow-capped peaks embracing a serene panorama—a high-altitude sanctuary."

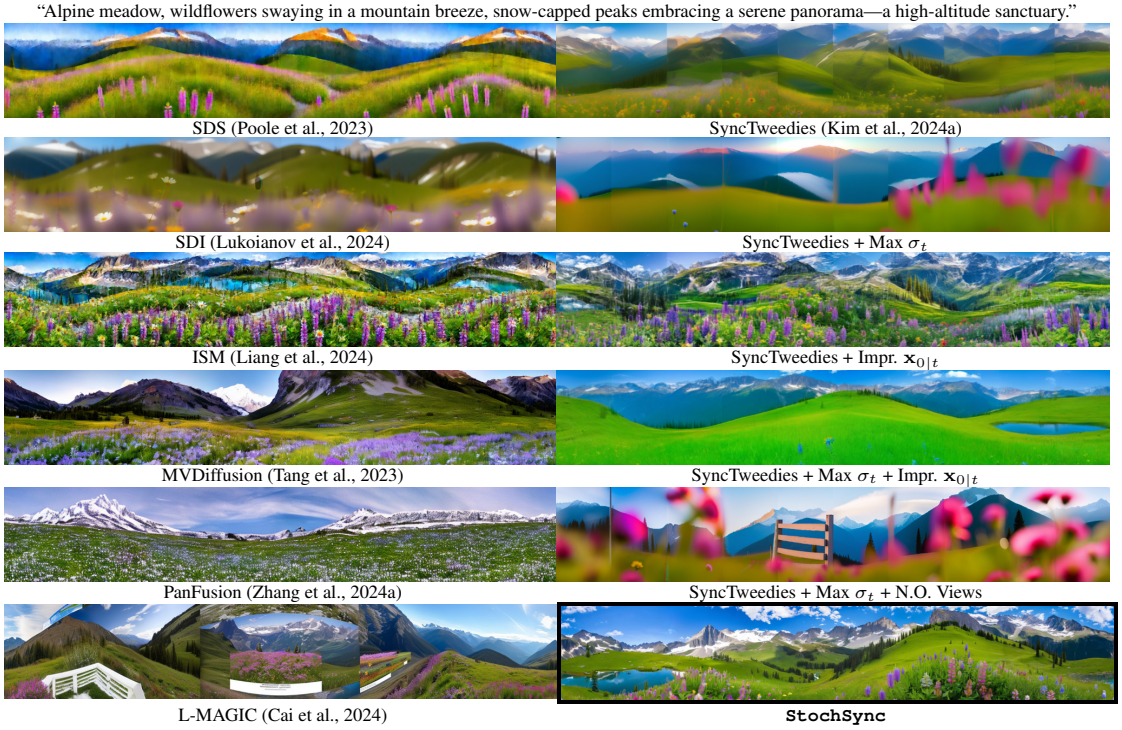

"Alpine village, snow-covered rooftops, nestled between majestic peaks—a picture-perfect scene of winter tranquility."

"Inside a floating city above the clouds, suspended by levitating platforms and connected by intricate sky bridges."

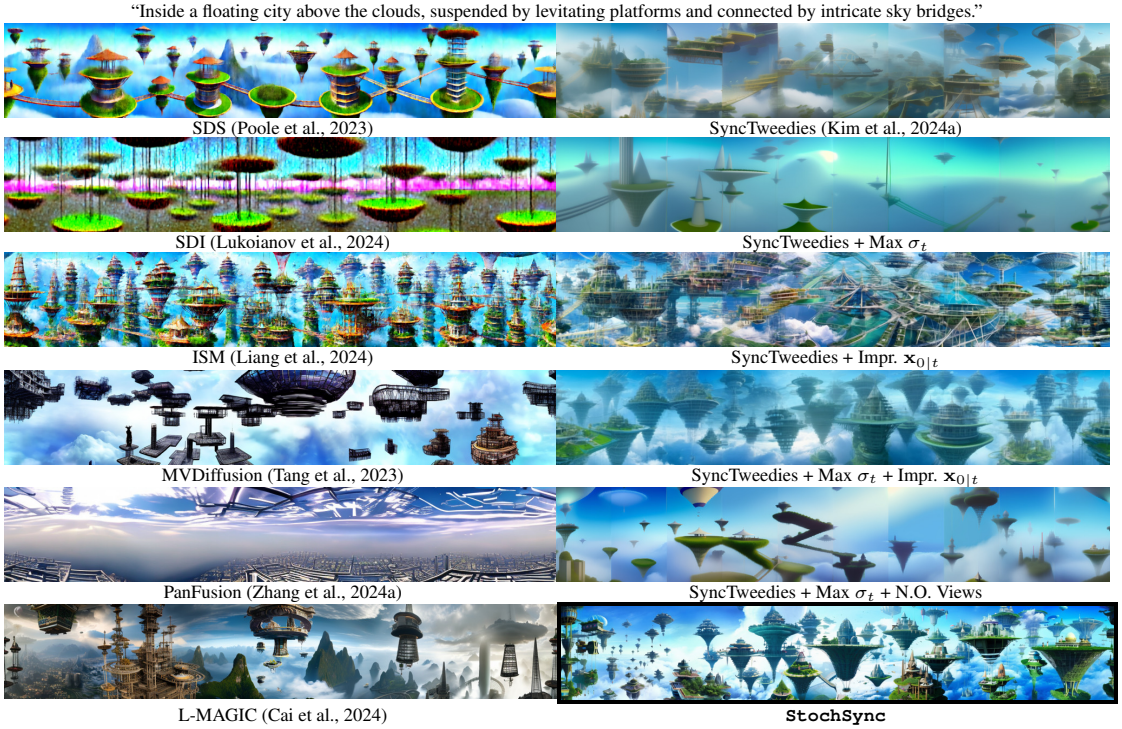

"Desert canyon, ancient rock formations sculpted by time, a vast expanse of terracotta hues—an arid symphony of textures."

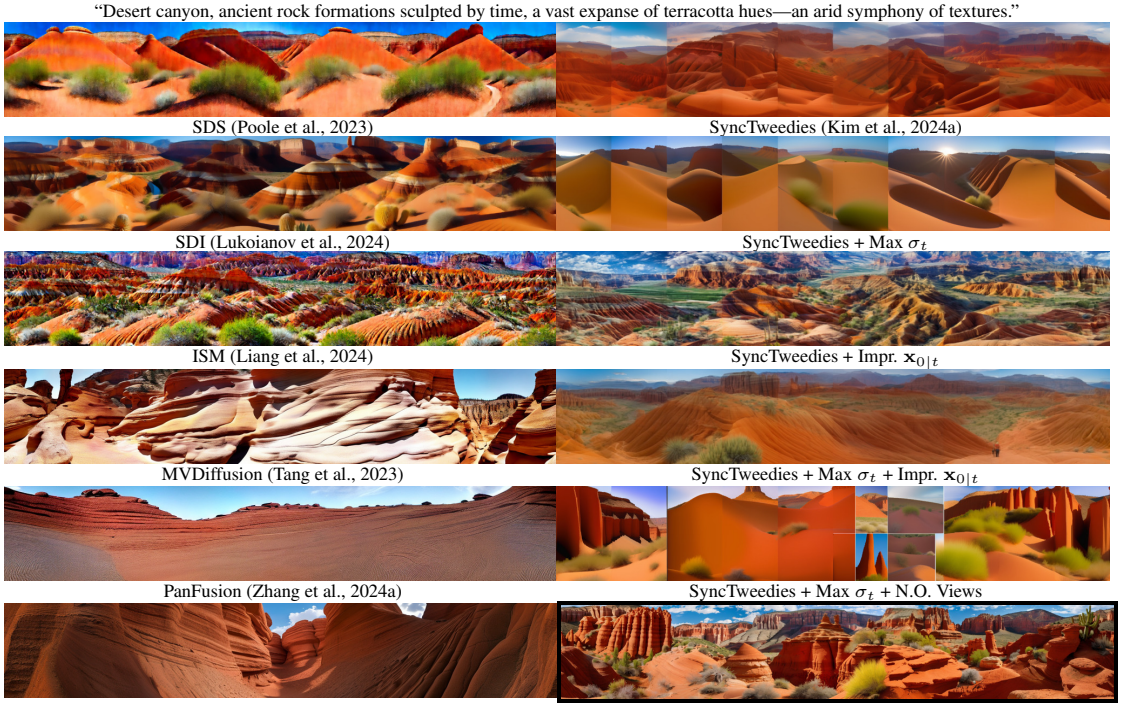

"Standing on the edge of a cliff, overlooking a vast desert landscape with towering sand dunes and a distant oasis."

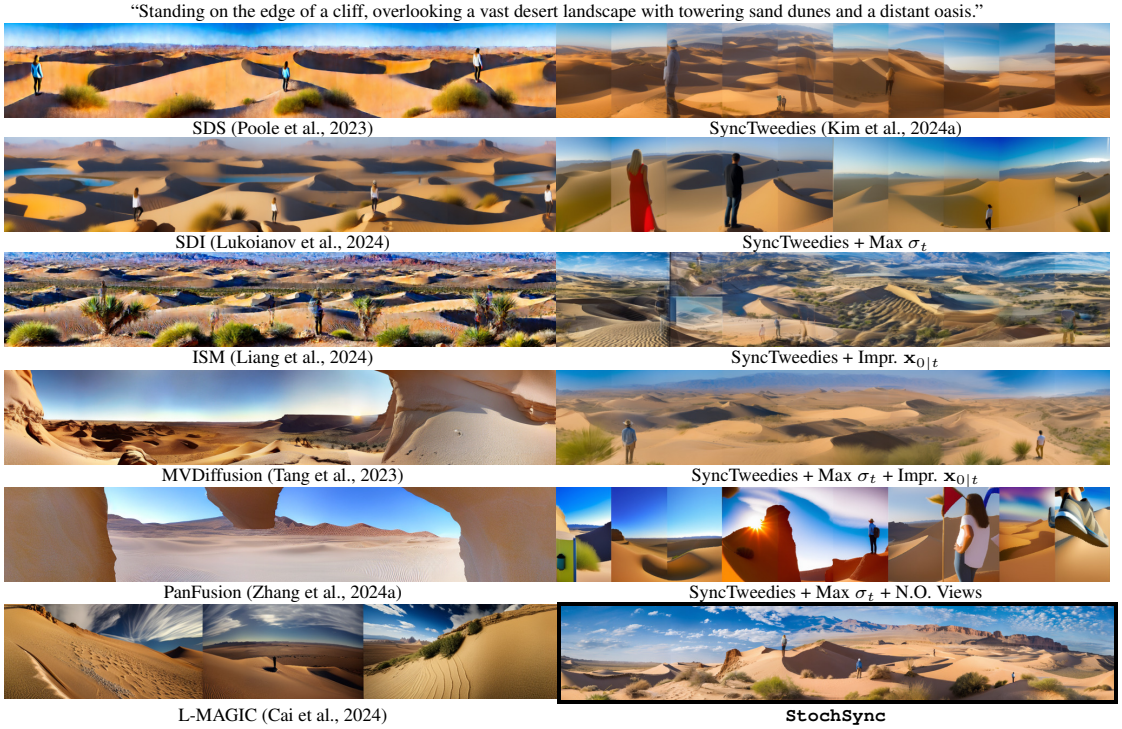

G.2 More 360° Panorama Generation Results Using L-MAGIC Prompts

"Desert under starlit sky"

SDS (Poole et al., 2023) | SyncTweedies (Kim et al., 2024a)

SDI (Lukoianov et al., 2024) | SyncTweedies + Max σ_t

ISM (Liang et al., 2024) | SyncTweedies + Impr. $\mathbf{x}_{0|t}$

MVDiffusion (Tang et al., 2023) | SyncTweedies + Max σ_t + Impr. $\mathbf{x}_{0|t}$

PanFusion (Zhang et al., 2024a) | SyncTweedies + Max σ_t + N.O. Views

L-MAGIC (Cai et al., 2024) | **StochSync**

"Snowy mountain peak view"

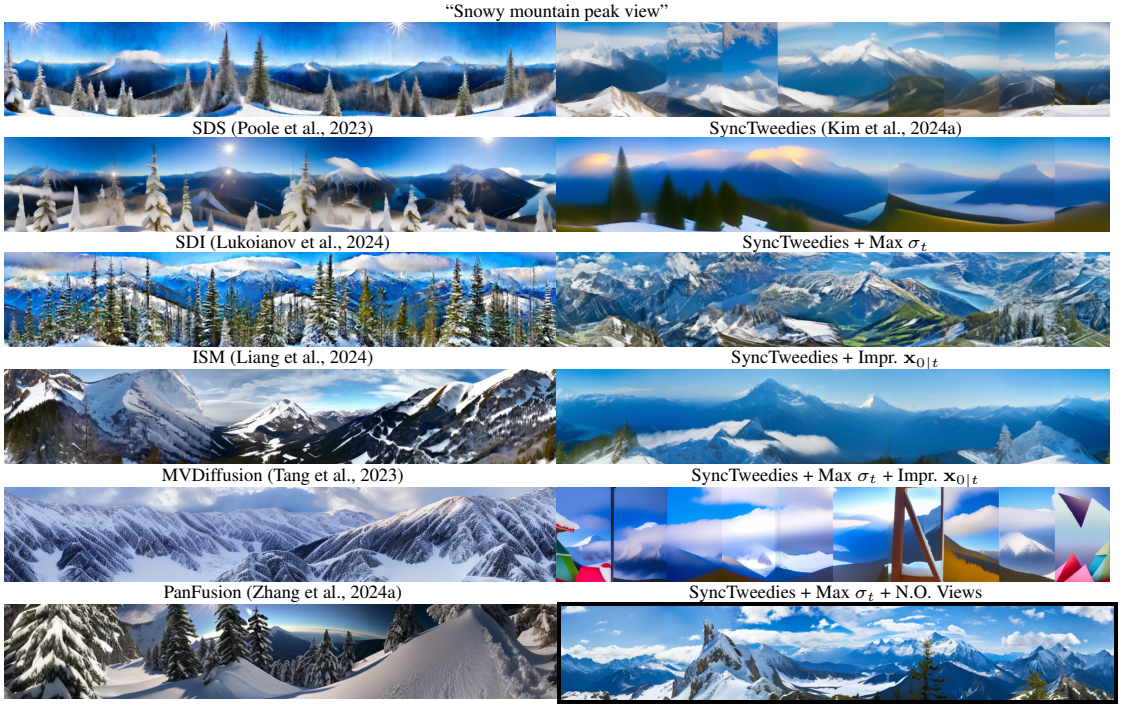

SDS (Poole et al., 2023) | SyncTweedies (Kim et al., 2024a)

SDI (Lukoianov et al., 2024) | SyncTweedies + Max σ_t

ISM (Liang et al., 2024) | SyncTweedies + Impr. $\mathbf{x}_{0|t}$

MVDiffusion (Tang et al., 2023) | SyncTweedies + Max σ_t + Impr. $\mathbf{x}_{0|t}$

PanFusion (Zhang et al., 2024a) | SyncTweedies + Max σ_t + N.O. Views

L-MAGIC (Cai et al., 2024) | **StochSync**

"Japanese Zen meditation room"
SDS (Poole et al., 2023)
SyncTweedies (Kim et al., 2024a)
SDI (Lukoianov et al., 2024)
SyncTweedies + Max σ_t
ISM (Liang et al., 2024)
SyncTweedies + Impr. $\mathbf{x}_{0|t}$
MVDiffusion (Tang et al., 2023)
SyncTweedies + Max σ_t + Impr. $\mathbf{x}_{0|t}$
PanFusion (Zhang et al., 2024a)
SyncTweedies + Max σ_t + N.O. Views
L-MAGIC (Cai et al., 2024)
StochSync

"Sakura blossom park Kyoto"
SDS (Poole et al., 2023)
SyncTweedies (Kim et al., 2024a)
SDI (Lukoianov et al., 2024)
SyncTweedies + Max σ_t
ISM (Liang et al., 2024)
SyncTweedies + Impr. $\mathbf{x}_{0|t}$
MVDiffusion (Tang et al., 2023)
SyncTweedies + Max σ_t + Impr. $\mathbf{x}_{0|t}$
PanFusion (Zhang et al., 2024a)
SyncTweedies + Max σ_t + N.O. Views
L-MAGIC (Cai et al., 2024)
StochSync